Isotopic coherence of refractory inclusions from CV and CK meteorites: Evidence from multiple isotope systems

Quinn R. Shollenberger[a,b*], Lars E. Borg[b], Jan Render[a], Samuel Ebert[a], Addi Bischoff[a], Sara S. Russell[c], Gregory A. Brennecka[a]

a. Institut für Planetologie, Westfälische Wilhelms-Universität, Wilhelm-Klemm-Straße 10, Münster 48149 Germany.
b. Nuclear & Chemical Sciences Division, Lawrence Livermore National Laboratory, 7000 East Avenue L-231, Livermore, CA 94550 USA.
c. Department of Earth Sciences, Natural History Museum, Cromwell Road, Kensington, London SW7 5BD, UK.

*Corresponding author
e-mail: shollenberger@wwu.de
phone: +49 251 83 36377
fax: +49 251 83 3601

To be submitted to *Geochimica et Cosmochimica Acta*

Abstract: 246 Words
Main text: 8492 Words
7 Tables
13 Figures

Abstract

Calcium-aluminum-rich inclusions (CAIs) are the oldest dated materials in the Solar System and numerous previous studies have revealed nucleosynthetic anomalies relative to terrestrial rock standards in many isotopic systems. However, most of the isotopic data from CAIs has been limited to the Allende meteorite and a handful of other CV3 chondrites. To better constrain the isotopic composition of the CAI-forming region, we report the first Sr, Mo, Ba, Nd, and Sm isotopic compositions of two CAIs hosted in the CK3 desert meteorites NWA 4964 and NWA 6254 along with two CAIs from the CV3 desert meteorites NWA 6619 and NWA 6991. After consideration of neutron capture processes and the effects of hot-desert weathering, the Sr, Mo, Ba, Nd, and Sm stable isotopic compositions of the samples show clearly resolvable nucleosynthetic anomalies that are in agreement with previous results from Allende and other CV meteorites. The extent of neutron capture, as manifested by shifts in the observed ^{149}Sm-^{150}Sm isotopic composition of the CAIs is used to estimate the neutron fluence experienced by some of these samples and ranges from 8.40×10^{13} to 2.11×10^{15} n/cm^2. Overall, regardless of CAI type or host meteorite, CAIs from CV and CK chondrites have similar nucleosynthetic anomalies within analytical uncertainty. We suggest the region that CV and CK CAIs formed was largely uniform with respect to Sr, Mo, Ba, Nd, and Sm isotopes when CAIs condensed and that CAIs hosted in CV and CK meteorites are derived from the same isotopic reservoir.

1. Introduction

Calcium-aluminum-rich inclusions (CAIs) are the first solids to condense in the cooling protoplanetary disk and mark the beginning of Solar System history. Therefore, these refractory inclusions provide constraints on the composition of some of the earliest reservoir(s) present in the Solar System. CAIs condensed at about 4.567 Ga (Amelin et al., 2010; Bouvier et al., 2011; Connelly et al., 2012), and most CAIs have an inferred initial ^{26}Al/^{27}Al ratio of ~5×10^{-5} which is used to define the short time interval for CAI formation, perhaps even as short as ~50,000 years (Bizzarro et al., 2004; Jacobsen et al., 2008; MacPherson et al., 2012). As such, these early solids represent a snapshot of the isotopic composition at the very start of the Solar System and contain clues to its early evolution. For instance, isotopic characterization of CAIs has demonstrated that they have isotopic anomalies in most elements when compared to later formed solids such as bulk chondrites and the terrestrial planets (see Dauphas and Schauble, 2016 for an extensive review on isotopic anomalies in CAIs). However, how the early Solar System evolved from the isotopic compositions measured in refractory inclusions to that of later formed solids, including chondrules and larger planetary bodies, remains unclear.

Refractory inclusions formed in the early Solar System include 1) hibonite-rich inclusions and 2) FUN (Fractionation and Unknown Nuclear effect) CAIs and 3) normal CAIs. Due to the large range of measured nucleosynthetic anomalies and non-canonical ^{26}Al/^{27}Al, hibonite-rich and FUN inclusions have been postulated to represent samples that formed prior to large-scale homogenization of the CAI-forming region (Wood, 1998; Sahijpal and Goswami, 1998; Kööp et al., 2016). As such, normal CAIs may represent a direct link between the CAI-forming region and later formed solids even though they have different nucleosynthetic anomalies. Therefore, whereas hibonite-rich and FUN inclusions are important for understanding the earliest history of the CAI-forming region, the focus of this study is on the far more abundant "normal" CAIs—hereafter referred to simply as CAIs—and their relationship to early Solar System reservoirs.

Nucleosynthetic anomalies in CAIs have been reported in many elements including: Ca, Ti, Cr, Ni, Sr, Zr, Mo, Ba, Nd, Sm, Hf, and W (e.g., Papanastassiou 1986; Birck and Lugmair, 1988; Trinquier et al., 2009; Sprung et al., 2010; Burkhardt et al., 2011; Huang et al., 2012; Moynier et al., 2012; Akram et al., 2013; Brennecka et al., 2013; Hans et al., 2013; Paton et al., 2013; Bermingham et al., 2014; Burkhardt et al., 2016; Bouvier and Boyet, 2016). Although there are some exceptions (e.g., Sprung et al., 2010; Burkhardt et al., 2011; Akram et al., 2013; Kruijer et al., 2014; Peters et al., 2017), broadly speaking, most CAIs have uniform and distinct nucleosynthetic anomalies indicating formation in a homogenous region (Brennecka et al., 2013). However, to this point, the vast majority of CAI isotopic studies examining elements above the Fe-peak have been limited to focusing solely on inclusions from Allende and a select few CAIs from other CV3 chondrites. It remains unknown if Allende CAIs are isotopically representative of all CAIs in all groups of meteorites, or if there are isotopic differences between host meteorites or meteorite classes. Therefore, isotopic analyses of different types of CAIs from other chondrite groups are of key importance for understanding the isotopic composition of the CAI-forming region as a whole.

The elements Sr, Mo, Ba, Nd, and Sm are well-suited to examine possible heterogeneities within the CAI-forming region because of their ample abundance in CAIs and the number of stable isotopes of each element. The individual isotopes of these five elements are produced by varying amounts of the *p*-, *s*-, and *r*-process nucleosynthesis pathways making them suitable to compare isotopic compositions of various CAIs. However, to this point, the sum of nucleosynthetic data from non-Allende CAIs in these elements derives from a total of seven combined measurements from Sr, Nd, and Sm (Paton et al., 2013; Hans et al., 2013; Bouvier and Boyet, 2016), with no data reported from CAIs from CK meteorites. Therefore, in order to more accurately characterize the CAI-forming region, we measured Sr, Mo, Ba, Nd, and Sm isotopes of two CAIs from CV3 chondrites and for the first time two CAIs from CK3 chondrites. This CAI isotopic data is then used to evaluate the degree of isotopic heterogeneity in the CAI-forming region with respect to Sr, Mo, Ba, Nd, and Sm.

2. Samples and methods

2.1 Samples investigated

2.1.1 Sample preparation

This study utilized four CAIs from four carbonaceous chondrites: two from the CV3 chondrites Northwest Africa (NWA) 6619 and NWA 6991 and two from the CK3 chondrites NWA 4964 and NWA 6254. The four samples were purchased from meteorite dealers and all derived from NWA meteorite finds. All four CAIs (designated as Lisa, Bart, Marge, and Homer) were roughly 1 cm in diameter and were more than 50 mg after removal from the host meteorites, enabling multiple isotopic systems to be studied (see Table 1 for specific sample information). Large CK CAIs are not common (e.g., Keller et al., 1992), meaning that the two CK CAIs from this study represent a rare opportunity for an integrated isotopic investigation. The samples were carefully removed from their respective meteorites using small hand tools wrapped in parafilm to minimize addition of terrestrial blank. In order to have enough sample material for the isotopic work, most of the CAI extracted from the meteorite was saved for those analyses and care was taken that matrix material was not included in these portions. Smaller pieces of the CAIs were set aside for petrographic investigation and elemental characterization. Fragments of each CAI were embedded in epoxy and polished as thick sections for petrographic work.

Table 1. Samples used for elemental and isotopic investigation in this study.

CAI	Host Meteorite	Mass (mg)	Description
Lisa	NWA 6991 (CV3)	53.4	B1, coarse-grained
Bart	NWA 6254 (CK3)	68.6	Type C*, coarse-grained
Marge	NWA 6619 (CV3)	111.7	Type B*, coarse-grained
Homer	NWA 4964 (CK3)	136.1	Type C*, coarse-grained

*Indicates the CAIs are anomalous examples most closely related to the indicated type. This is due to the unusual mineralogy of these inclusions (e.g., containing Fa-rich olivine, abundant grossular) partly reflecting secondary modifications.

2.1.2 Sample petrology and mineralogy

A JEOL 6610-LV electron microscope (SEM) at the Interdisciplinary Center for Electron Microscopy and Microanalysis (ICEM) at the University of Münster was used to examine the textures of the four CAIs and to identify the mineral phases present in the CAIs. Quantitative mineral and bulk chemical analyses were obtained using a JEOL JXA 8900 Superprobe electron microprobe (EPMA) at the ICEM, which was operated with five spectrometers at 15 kV and a probe current of 15 nA. Natural and synthetic standards were used for wavelength dispersive spectrometry. Jadeite (Na), kyanite (Al), sanidine (K), chromium oxide (Cr), San Carlos olivine (Mg), hypersthene (Si), diopside (Ca), rhodonite (Mn), rutile (Ti), fayalite (Fe), cobalt metal (Co), willemite (Zn), and nickel oxide (Ni) were used as standards for bulk and mineral analyses. For mineral analysis, a beam diameter of ~1-8 µm (depending on mineral size) was used and Na was analyzed in the first analytic cycle in order to avoid Na-loss due to volatilization under the beam. The bulk compositions were obtained using a defocused beam of 50 µm. The microprobe data were corrected according to the $\Phi\rho(z)$ procedure (Armstrong, 1991). The basic mineralogical characteristics of each inclusion are summarized below, and bulk chemical and mineral compositional data of the CAIs are given in the electronic annex (Tables EA1 and EA2).

Lisa is a coarse-grained, Type B1, CAI from the NWA 6991 $CV3_{ox}$ chondrite and the texture is shown in Fig. 1. The boundary to the fine-grained host matrix of the chondrite is defined by a Wark-Lovering rim (Wark and Lovering, 1977), mainly consisting of an outer portion of Al-bearing diopside and an inner spinel-rich layer containing small embedded perovskite grains. A thick (~800 µm) mantle of melilite is present within the CAI (Fig. 1) with an Åk-content ranging from 15 to 51 mol%. Within the interior of the CAI, fassaite grains up to 1 mm in size are present and have variable concentrations of TiO_2 (6-12 wt%) and Al_2O_3 (16-19 wt%). Both melilite and fassaite poikilitically enclose small euhedral spinel grains. Additionally, tiny opaque Fe,Ni-sulfides and Pt,Fe,Ni-rich particles are found.

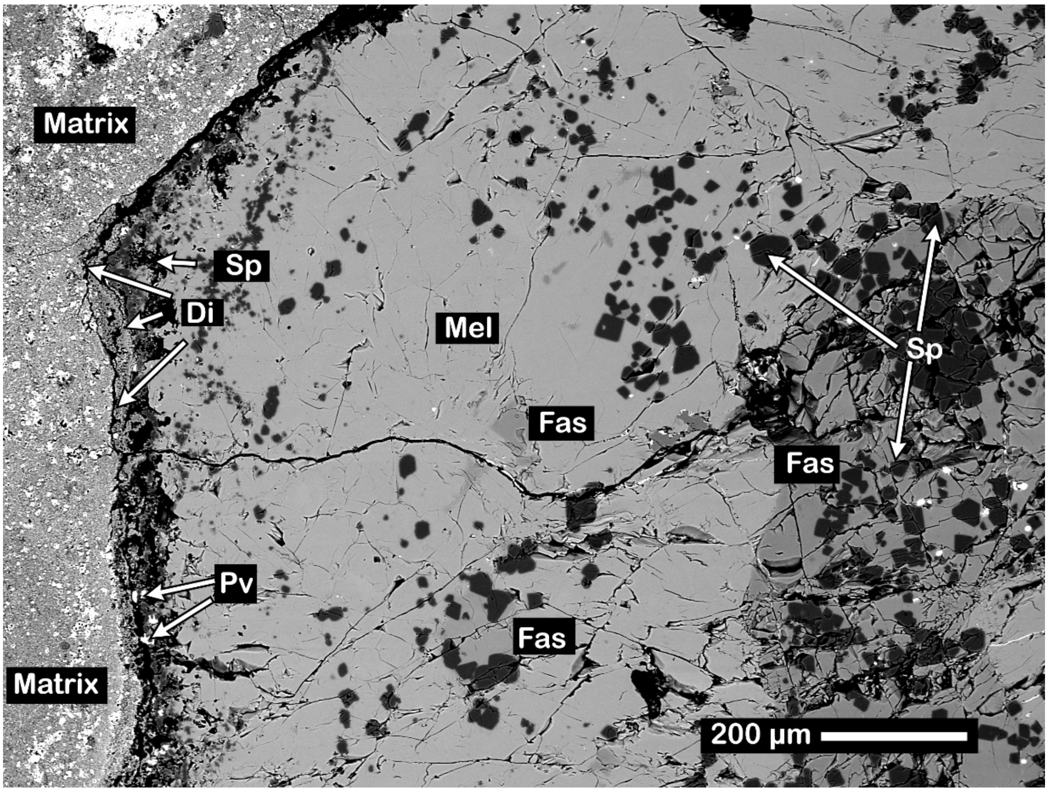

Figure 1. Photomicrograph of a typical area of the Lisa CAI from the CV3 chondrite NWA 6991 illustrating abundant melilite (Mel) and fassaite (Fas) poikilitically enclosing spinel grains (Sp). The inclusion is rimed by porous layers of diopside (Di) and spinel, containing small perovskite grains (Pv). The tiny bright phases are Fe,Ni-sulfides and Pt,Fe,Ni-rich particles. Image in back-scattered electrons.

Bart is a CAI from the CK3 chondrite NWA 6254 and is most closely related to Type C CAIs. Two small fragments of Bart were characterized petrologically and although both fragments contain abundant plagioclase, the fragments have different textures and mineralogies. One fragment consists of abundant olivine laths (~Fa_{33-34}) that are paragenetic with two generations of plagioclase, indicative of secondary alteration. Ca-rich plagioclase ($An_{>80}$, often $An_{>90}$) is surrounded by more Na-rich plagioclase (oligoclase-andesine; ~An_{19-45}), as shown in Fig. 2a. Opaque phases, such as Ti-bearing magnetite and ilmenite, are present. The second fragment consists of lath-like low-Ca pyroxene (~Fs_{23-24}) and minor olivine (Fa_{28-31}; Fig. 2b). Again, two generations of plagioclase (mainly $An_{>90}$ vs. ~An_{35-55}) exist, as well as minor grossular. The An-rich plagioclase and olivine contain abundant small Fe-rich particles that are likely magnetite and ilmenite.

The Fa-content of olivine and Fs-content of low-Ca pyroxene in Bart, as well as the concentration of ~0.3 wt% NiO in olivine are typical mineral-chemical features for CK chondrites (Geiger and Bischoff, 1995). Olivine measurements of the NWA 6254 bulk rock revealed $Fa_{30.7\pm8.3}$ (Fa_{0-35}; N=21; *Meteoritical Bulletin Database* 2016) and are consistent with a 3.7-subtype classification (see Scott, 1984 for details). Therefore, the classification of this meteorite is consistent with thermal metamorphism on the parent body which most likely caused the unique mineralogy of Bart as described above.

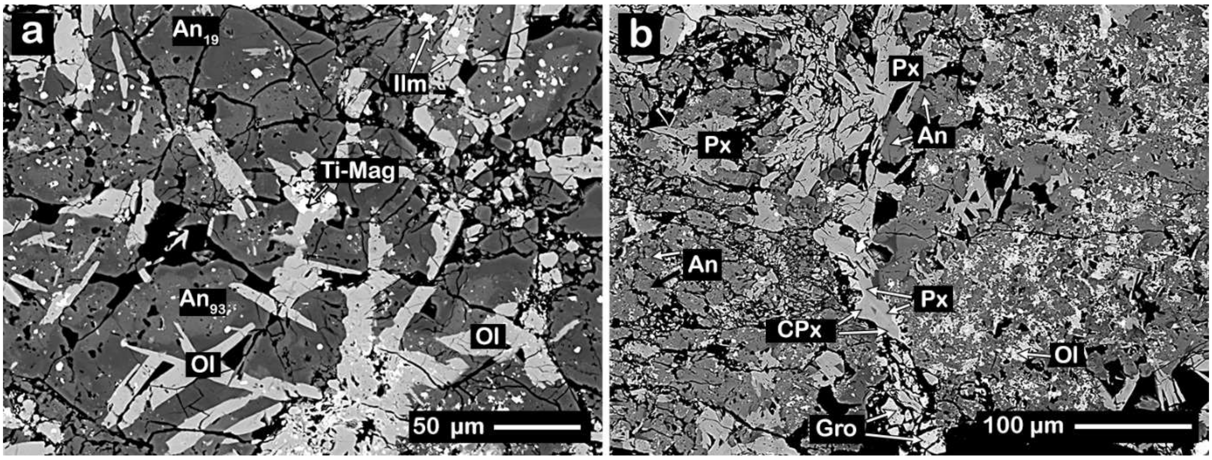

Figure 2. Textural and mineralogical characteristics of two parts of the Bart CAI from the CK3 chondrite NWA 6254. (a) This area of Bart consists of olivine laths (Ol) embedded within an intergrowth of two chemically different plagioclase phases, which are distinguished based on their An-contents. (b) The second area consists of lath-like low-Ca pyroxene (Px), abundant An-rich plagioclase (An), and minor olivine, Ca-pyroxene (CPx), and grossular (Gro). The bright phases in both images are magnetite (Mag) and ilmenite (Ilm). Images in back-scattered electrons.

The CAI Marge from the CV3 chondrite NWA 6619 is a unique Type B CAI that consists of abundant fassaite, some grossular, and minor anorthite ($An_{>98}$) (Fig. 3a). All three phases contain abundant euhedral to subhedral spinel and Fe-rich Ca-pyroxene (hedenbergite) occurs intergrown with grossular (Fig. 3a). The inclusion is rimmed by Fe-rich olivine, Ca-pyroxene (diopside), and a spinel-rich layer. The spinel at the rim of the inclusion is slightly zoned and contains minor Fe. The spinel within the anorthite are also zoned (Fig. 3b). Although the rims are too small for analysis, the outermost spinel appears to contain some Fe. On the other hand, this appearance might be due to the incorporation of some Ca from the surrounding anorthite. Marge also contains a shock vein along with areas (veins) filled with secondary terrestrial contaminants (calcites, quartz).

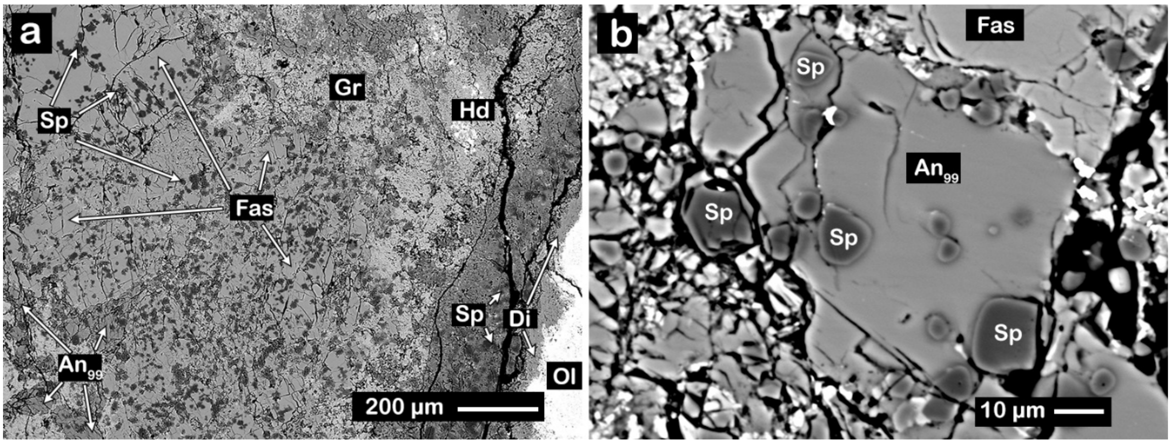

Figure 3. Textural and mineralogical characteristics of the CAI Marge. (a) The inclusion is extremely fractured and contains abundant fassaite (Fas), less grossular (Gr), and minor anorthite (An). Small euhedral to subhedral spinel (Sp) occur in all three phases (dark grains). The white minerals on the right-hand side are hedenbergite (Hd). Marge is rimmed by Fe-rich olivine (Ol; white outer boundary), Ca-pyroxene (diopside; Di), and a spinel-rich layer. (b) Spinel within the anorthite are zoned. Images in back-scattered electrons.

Homer is hosted in the CK3 chondrite NWA 4964 and is most closely related to Type C CAIs. This is a very complex CAI having areas with different mineral paragenesis. It consists of abundant anorthite ($An_{>95}$) embedding grossular, Ca-pyroxenes (Fig. 4a), Fe-rich spinel (19-28 wt% FeO) and hibonite-spinel (Fig. 4b) or corundum-spinel (Fig. 5) intergrowths. Some of the spinel are rich in ZnO (>5 wt%). Measurements of olivine compositions in the matrix of the bulk meteorite have $Fa_{30.7\pm5.9}$ ($Fa_{13\text{-}35}$; N=22; *Meteoritical Bulletin Database* 2016) indicating thermal metamorphism consistent with a 3.8-subtype classification. Tiny grains of ilmenite are scattered throughout the inclusion, which likely formed during secondary processing in the solar nebula or on the meteorite parent body by metamorphic processes as replacement products of preexisting perovskite. In some cases, perovskite is enclosed in spinel and survived complete transformation into ilmenite. Multiple grains of corundum, which are extremely rare in CAIs, were found up to 200 µm in length (Fig. 5b) and are the largest corundum grains ever reported in CAIs (e.g., Kurat, 1970; Bar-Matthews et al., 1982; Wark, 1986; Bischoff and Palme, 1987; Simon et al., 2002; Makide et al., 2011; Russell and Kearsley, 2011). Within Homer, the corundum grains often coexist with grossular, Fe-rich spinel, and plagioclase (sometimes having Ab-contents up to 52 mol%; Fig. 5a).

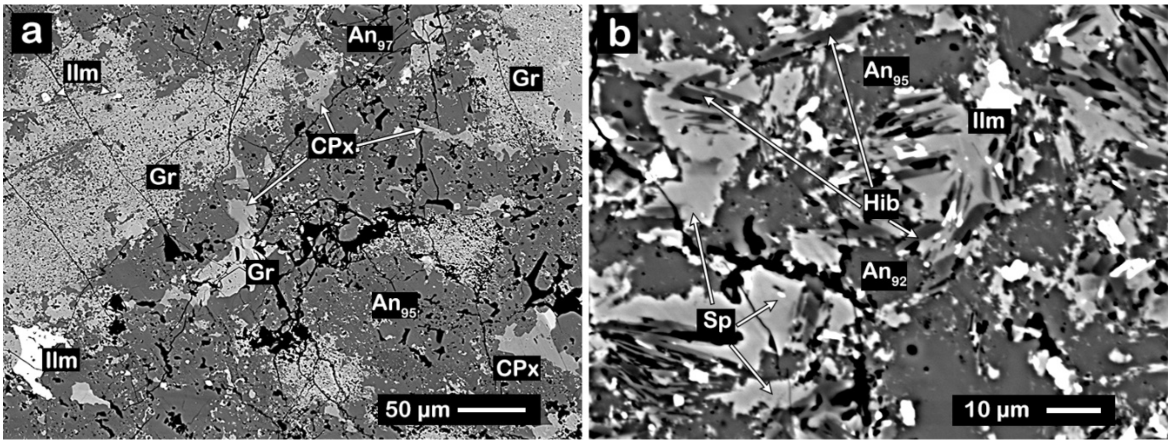

Figure 4. Textural and mineralogical characteristics of the Homer CAI. (a) Anorthite (dark grey, An) is enclosing grossular-rich areas as well as Ca-pyroxene (CPx), and a large ilmenite grain (Ilm). (b) Hibonite (dark laths, Hib) are intergrown with Fe-rich spinel (Sp) and both are embedded in An-rich plagioclase. Small ilmenite particles and minor tiny Ti-bearing magnetite (or titanomagnetite) grains (light phases in both images) are scattered throughout the inclusion. Images in back-scattered electrons.

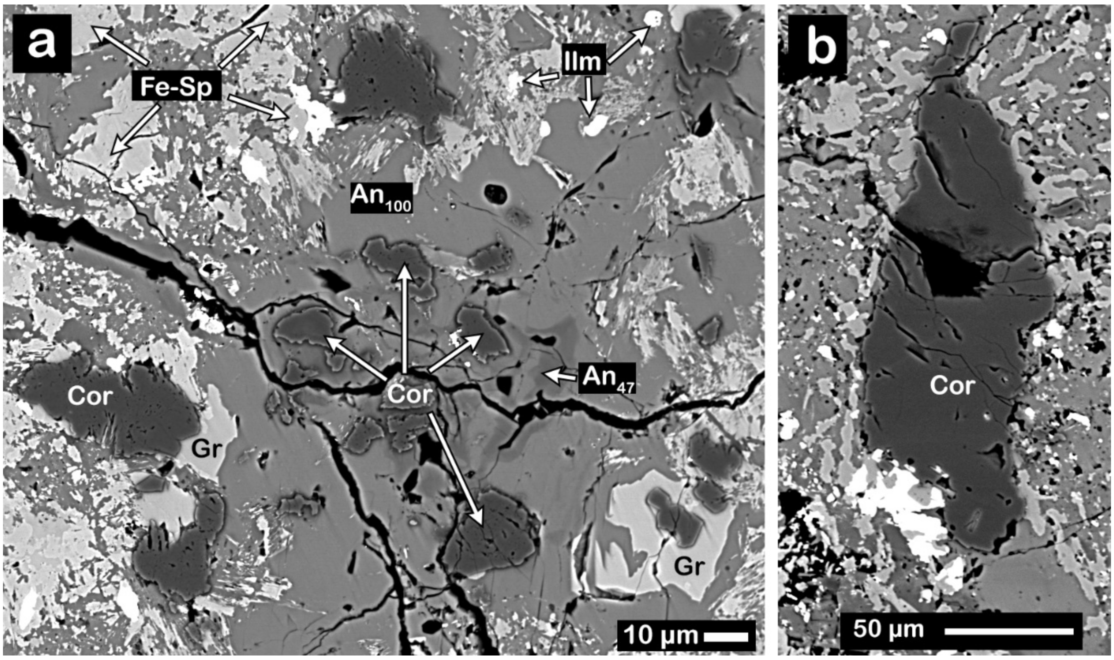

Figure 5. (a) Several large corundum grains (black) in the Homer CAI intergrown and/or associated with grossular (Gr) and Fe-rich spinel (Fe-Sp). They are mainly enclosed by anorthitic plagioclase, but in the center they are also in contact with andesine (~An_{47}). The bright phases are ilmenites. (b) The largest corundum grain ever reported in CAIs. Images in back-scattered electrons.

2.2 Sample digestion and chemical separation of Sr, Mo, Ba, Nd, and Sm

The sample aliquots used for isotopic work were ground into a fine powder using a sapphire mortar and pestle. The samples were digested in Parr bombs at Lawrence Livermore National Laboratory (LLNL) using concentrated HNO_3, and HF. Multiple treatments of aqua regia was necessary following Parr bomb digestion in order to completely dissolve the samples. The samples were fluxed in 2 mL of 0.5N HCl-0.15N HF and 2% of this solution was removed for ICPMS trace element analysis. Following the procedure of Connelly et al. (2006), Mo and other high field strength elements (HFSE) were separated from the CAI solutions using columns containing 2 mL of AG50W-X8 cation-exchange resin (200-400 mesh) and 3 mL of 0.5N HCl-0.15N HF acids. The rest of the CAI matrix containing Sr, Ba, and the rare earth elements (REEs) was eluted in 6N HCl in preparation for subsequent purification.

Molybdenum was separated and purified from the HFSEs using a three-stage ion exchange chemistry following the procedure from Render et al. (2017). Briefly, the HFSE solutions in 1M HCl-0.1M HF were first passed through a column containing 14 mL pre-cleaned AG50W-X8 (200-400 mesh) cation-exchange resin to remove any remaining major elements from the HFSE solutions. Next, the HFSE solutions were loaded onto columns filled with 2 mL of pre-cleaned AG1-X8 (100-200 mesh) anion-exchange resin to remove any remaining Fe, Ni, Ti, and W as well as most of the Zr and Ru. This column utilized 1M HF, 6M HCl-0.06M HF, 6M HCl-1M HF, and H_2O, and Mo was eluted in 3M HNO_3 and H_2O. Finally, Mo was purified on a third column containing 1 mL of pre-cleaned Eichrom® TRU-Spec cation resin (100-200 mesh) using 7M HNO_3 and Mo is eluted in 0.1M HNO_3. The final Mo cuts were dried down and treated with a few drops of concentrated HNO_3 and HCl to decompose remaining organic matter. Molybdenum blanks for this separation procedure are typically 0.8 ± 0.5 ng and do not significantly affect the Mo isotopic compositions given that >75 ng Mo were processed for each CAI sample.

Strontium, Ba, and the REEs were separated from the CAI matrix based on methods outlined in Carlson et al. (2007). In short, a cation-exchange resin (AG50W-X8, 200-400 mesh) was used to elute Sr, Ba, and the REEs using 2N HCl, 2N HNO_3, and 6N HCl, respectively. Strontium was further purified using Eichrom® Sr-spec resin based on the procedure from Andreasen and Sharma (2007). The REEs were loaded onto pressurized 0.2M alpha-hydroxyisobutyric acid columns based on the procedure from Borg et al. (2016) in order to separate and purify Nd and Sm. Two passes were necessary for precise Nd isotopic ratio measurements. After the pressurized column, a 2 mL cation exchange (AG50W-X8, 200-400 mesh) clean-up chemistry was necessary to remove the alpha-hydroxyisobutyric acid from the Nd and Sm cuts.

2.3 Trace element measurements

Trace element concentrations were obtained on a Thermo Scientific® iCAP Q quadruple at LLNL. The pre-chemistry aliquots were diluted appropriately with 2% HNO_3 in preparation for ICPMS measurements. A dissolved aliquot of the geological rock standard BHVO-2 was measured with the CAIs at different concentrations and was used for calibration. All measurement solutions were doped with an internal standard to monitor and correct for instrumental drift. Trace element data can be found in Table EA3.

2.4 Isotopic measurements

Isotopic measurements for Sr, Ba, Nd, and Sm of the samples and standards were completed at LLNL using a Thermo Scientific® Triton thermal ionization mass spectrometer. The Mo isotopic compositions were measured in the Institut für Planetologie at the University of Münster using a Thermo Scientific® Neptune *Plus* MC-ICPMS. Data for all elements are reported in the ε-notation, or parts per 10,000 deviations relative to terrestrial standards. The measurement protocol of this study was very similar to the measurement specifics reported in Brennecka et al. (2013) with a few minor differences as indicated below.

For Sr, approximately 1 µg of each sample/standard was loaded in 2N HCl onto single Re filaments along with the Ta_2O_5 activator in phosphoric acid. Strontium isotopic measurements for the samples and standards were static runs consisting of 200 ratios using 16 second integration times. Each sample was measured two times on the same filament. The isobaric interfering element Rb was monitored by simultaneously measuring ^{85}Rb with the other Sr isotopes. Internal normalization was used to correct for mass bias effects using $^{86}Sr/^{88}Sr$ = 0.1194. The external reproducibility (2SD) of the $^{84}Sr/^{86}Sr$ ratio based on multiple analyses of the NBS 987 standard was ± 0.4ε.

Molybdenum isotope measurements were performed following the protocol from Render et al. (2017). Samples were introduced with a Savillex® C-Flow PFA nebulizer and Cetac® Aridus II desolvator, resulting in total ion beam intensities of ~1.3×10^{-10} A using 100 ppb solutions and an uptake rate of ~50 µl/min. Measurements consisted of an on-peak baseline on a solution blank for 40 integrations followed by 100 integrations of the sample solution both using 8 second integration times. Instrumental mass bias was corrected using the exponential law normalizing to $^{98}Mo/^{96}Mo$ = 1.453171 (Lu and Masuda, 1994). All Mo isotopes were monitored using 10^{11} ohm resistors and potential isobaric interferences from Zr and Ru on several Mo isotopes were quantified by monitoring signals on ^{91}Zr and ^{99}Ru in Faraday cups connected to amplifiers with 10^{12} ohm resistors. Based on the amount of Mo available, samples were run at either 100 ppb (Lisa, Bart) or 75 ppb (Homer, Marge).

Barium was loaded on zone-refined double Re filaments in 2N HCl and the amount of Ba loaded ranged from 0.3 to 1 µg, depending on the amount Ba in the sample. Barium was measured for 200 ratios in static mode using 16 second integration times and each sample was measured at least three times on the same filament. The interfering isotopes, ^{139}La and ^{140}Ce were monitored simultaneously with the Ba isotopes. The minor isotopes of Ba (^{130}Ba and ^{132}Ba) along with the isobaric interference ^{140}Ce were measured utilizing 10^{12} ohm resistors, where all other isotopes of Ba and the isobaric interference ^{139}La were measured using 10^{11} ohm resistors. The data were corrected for instrumental mass bias effects using $^{134}Ba/^{136}Ba$ = 0.3078 and the ^{138}Ba data was corrected for radiogenic ingrowth from ^{138}La as shown in Brennecka et al. (2013). The La/Ba ratios used for this correction are given in Table 4.

Neodymium was loaded on zone-refined double Re filaments in 2N HCl and depending on the sample size, 200-900 ng of Nd was loaded. The data acquisition was performed using a two-step dynamic measurement routine. Each dynamic run consisted of 540 ratios with each step of the routine using 8 second integration times. The interfering isotopes ^{140}Ce, ^{141}Pr, ^{147}Sm, and ^{149}Sm were all measured utilizing 10^{12} ohm resistors and all other Nd isotopes were measured with 10^{11} ohm resistors. The Nd measurements occurred during two different sessions with Lisa, Bart, and Marge measured during the first session and Homer measured several months later. Regardless of different measurement sessions, each sample was measured at least one time and the data were compared to the standards of their respective measurement campaign. All data are corrected for mass bias effects using $^{146}Nd/^{144}Nd$ = 0.7219 and the exponential law.

Approximately 125 – 300 ng of Sm was loaded onto zone-refined double Re filaments in 2N HCl. Samarium isotopic measurements were performed using a static routine with 8 second integration times and each run consisted of 200-300 ratios depending on the sample size. The interfering elements Nd and Gd were monitored using the isotopes ^{146}Nd and ^{155}Gd and were measured simultaneously during the run with 10^{12} ohm resistors whereas all Sm isotopes were measured using 10^{11} ohm resistors. Instrumental mass bias was corrected using ^{147}Sm/^{152}Sm = 0.56081 and the exponential law and this internal normalization scheme was selected to monitor potential neutron capture effects on ^{149}Sm and ^{150}Sm.

3. RESULTS

3.1 Rare earth element patterns

The REE patterns of the CAIs are calculated relative to CI chondrites (Lodders, 2003) and are displayed in Fig. 6. The CAIs have REE abundances of ~20×CI except Homer, which is less than 10×CI. Bart and Lisa have relatively flat REE patterns, although Bart has negative Eu and Yb anomalies which is consistent with the group III pattern (Martin and Mason, 1974). Marge has a slightly fractionated REE pattern while Homer, a coarse-grained CAI, has a fractionated REE pattern similar to the group II pattern which is characterized by having enrichments in the light REEs (La, Ce, Pr, Nd, Sm) along with depletions in the most refractory REEs (Gd, Tb, Dy, Ho, Er, Lu) (Mason and Martin, 1977). The group II pattern also has a negative Eu anomaly and a positive Tm anomaly and CAIs exhibiting such REE patterns are believed to have experienced complex condensation histories (Boynton, 1975; Davis and Grossman, 1979). However, Homer is depleted in the elements Eu-Ho and has an enrichment in Yb, although other group II patterns show similar enrichments for Yb. These differences may be an indication that Homer experienced several episodes of evaporation and condensation and the positive Yb anomaly probably reflects the volatile behavior of this element. Previous work noted that CAIs containing the typical group II pattern but having positive instead of negative Eu and Yb anomalies were designated as group IIA, thus demonstrating that variations within the group II pattern exist (Davis and Grossman, 1979). Furthermore, Homer's REE abundance is remarkably low overall for a CAI which also suggests a complex history that could also be indicative of interaction with chondrule material. This could also explain why Homer's composition is related to Type C which is the least refractory CAI type. Although Homer's REE pattern does not exactly match the description of group II CAIs, it is likely that Homer experienced a more complex formation history compared to other samples of this study.

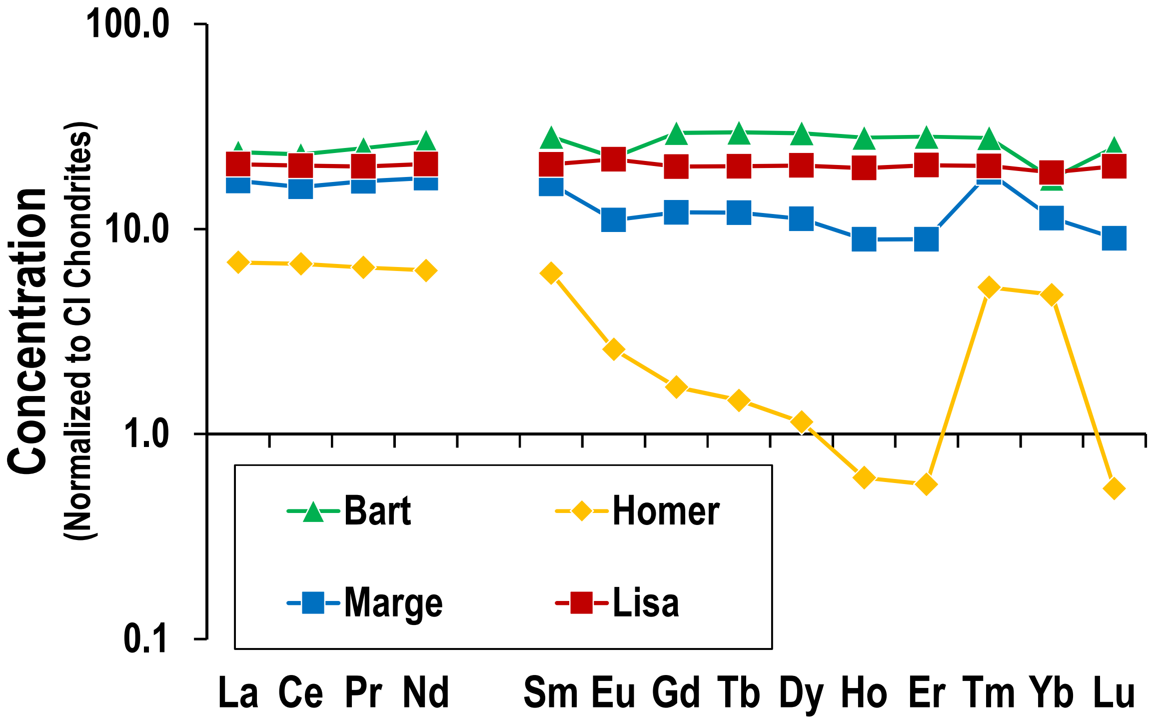

Figure 6. Rare Earth element patterns of the CAIs analyzed in this study. Bart, Marge and Lisa have relatively unfractionated REE patterns while Homer has a fractionated REE pattern similar to group II CAIs and indicative of a more complex condensation history. Data normalized to CI chondrites using Lodders (2003).

3.2 Isotopic compositions

All isotopic data are presented in ε-notation, or parts per 10,000 deviation from the terrestrial standards. For clarity, we have calculated an average Allende CAIs ε-value for each isotope ratio using literature data that is displayed in the figures (Harper et al., 1992; Burkhardt et al., 2011; Moynier et al., 2012; Hans et al., 2013; Brennecka et al., 2013; Bermingham et al., 2014; Burkhardt et al., 2016; Bouvier and Boyet, 2016). Details about the calculation for the average Allende CAIs values are given in the electronic annex (EA).

3.2.1 Sr isotopic compositions

The Sr isotopic compositions of the samples and standards are presented in Fig. 7 and Table 2. Strontium has four stable isotopes, however, two are used for internal normalization of the data (^{86}Sr and ^{88}Sr) and one (^{87}Sr) has significant radiogenic ingrowth from ^{87}Rb that is difficult to correct for at the required precision for nucleosynthetic study given the relatively large uncertainties on the measured ^{87}Rb/^{86}Sr ratios. Therefore, the main isotope of focus is ^{84}Sr. The ε^{84}Sr values are given relative to the NBS 987 standard and the external reproducibility (2 × standard deviation, 2SD) of the standard during the measurement campaign was 0.4 for ε^{84}Sr. Marge and Lisa have ε^{84}Sr excesses of 0.8 and 1.4 ε-units, respectively. These data resemble the previous results on Sr in CAIs (Moynier et al., 2012; Hans et al., 2013; Paton et al., 2013; Brennecka et al., 2013). Bart and Homer both have ε^{84}Sr excesses of 0.4 ε, which is within analytical uncertainty of both the terrestrial value and average Allende CAI value.

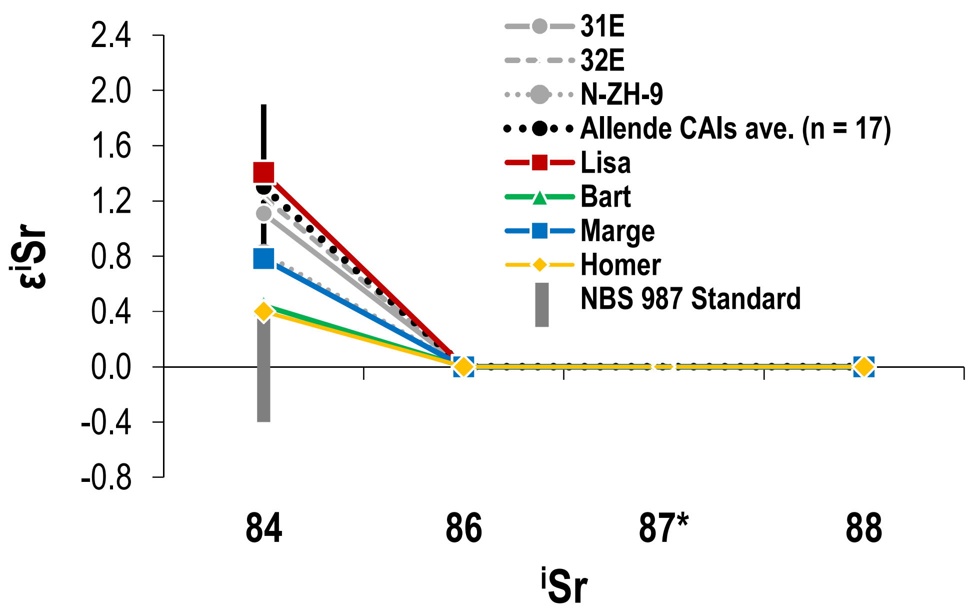

Figure 7. The Sr isotopic compositions of the CAIs analyzed in this study along with the calculated Allende CAI Sr average value (data from Moynier et al., 2012; Hans et al., 2013; Brennecka et al., 2013) and CAIs from non-Allende CV3 meteorites (Hans et al., 2013; Paton et al., 2013). The deviation of the samples relative to the terrestrial standard is given in ε-notation. The uncertainty on the standard (shown as a solid grey bar) in the plot represents 2 × standard deviation (2SD) of that standard during the measurement campaign. For clarity purposes, only the 2SD of the Allende CAIs average value is shown (black error bar).
*Denotes isotopic data not included due to radiogenic input

Table 2. The Sr isotopic ratios and other pertinent information of the standards and samples of this study.

Sample	Total ratios	~µg Sr Loaded	Volts ^{88}Sr	Normalized to $^{86}Sr/^{88}Sr$	$^{84}Sr/^{86}Sr$	$^{87}Sr/^{86}Sr$ meas.	$^{85}Rb/^{86}Sr$	$^{87}Sr/^{86}Sr$ corr.	$\varepsilon^{84}Sr$
Bart Average	400	1	6.5	**0.1194**	0.056495	0.699617	0.000002	0.699617	**0.4**
Homer Average	400	1	6.8	**0.1194**	0.056495	0.705680	0.000000	0.705680	**0.4**
Marge Average	400	1	6.3	**0.1194**	0.056497	0.703984	0.000004	0.703983	**0.8**
Lisa Average	400	1	6.2	**0.1194**	0.056501	0.699421	0.000007	0.699419	**1.4**
NBS-987 Average	1400	2	6.7	**0.1194**	0.056493	0.710246	0.000000	0.710246	**0.0**
2SD					0.000002	0.000010	0.000005	0.000011	**0.4**
Allende CAIs*									**1.3**
2SD									**0.6**

*See EA for details on the Allende CAIs calculation

3.2.2 Mo isotopic compositions

The Mo isotopic compositions of the samples and standards are presented in Fig. 8 and Table 3. The external reproducibility of the method was determined by multiple analyses (N = 24) of the terrestrial rock standard BHVO-2 and is 0.37 for $\varepsilon^{92}Mo$, 0.27 for $\varepsilon^{94}Mo$, 0.16 for $\varepsilon^{95}Mo$, 0.10 for $\varepsilon^{97}Mo$, and 0.19 for $\varepsilon^{100}Mo$. Bart and Lisa both show resolved excesses in all five Mo isotopes and their patterns resemble previous results for Mo in coarse-grained CAIs from Allende (Yin et al., 2002; Becker and Walker, 2003; Burkhardt et al., 2011; Brennecka et al., 2013). However, only Bart fits the average Allende CAI pattern within analytical uncertainty on all isotopes and although Lisa has smaller Mo isotopic anomalies, the overall pattern is similar to previous Allende CAI data. Marge and Homer both have near terrestrial Mo isotopic compositions although Marge hints at Mo isotope excesses except for ε^{100}Mo.

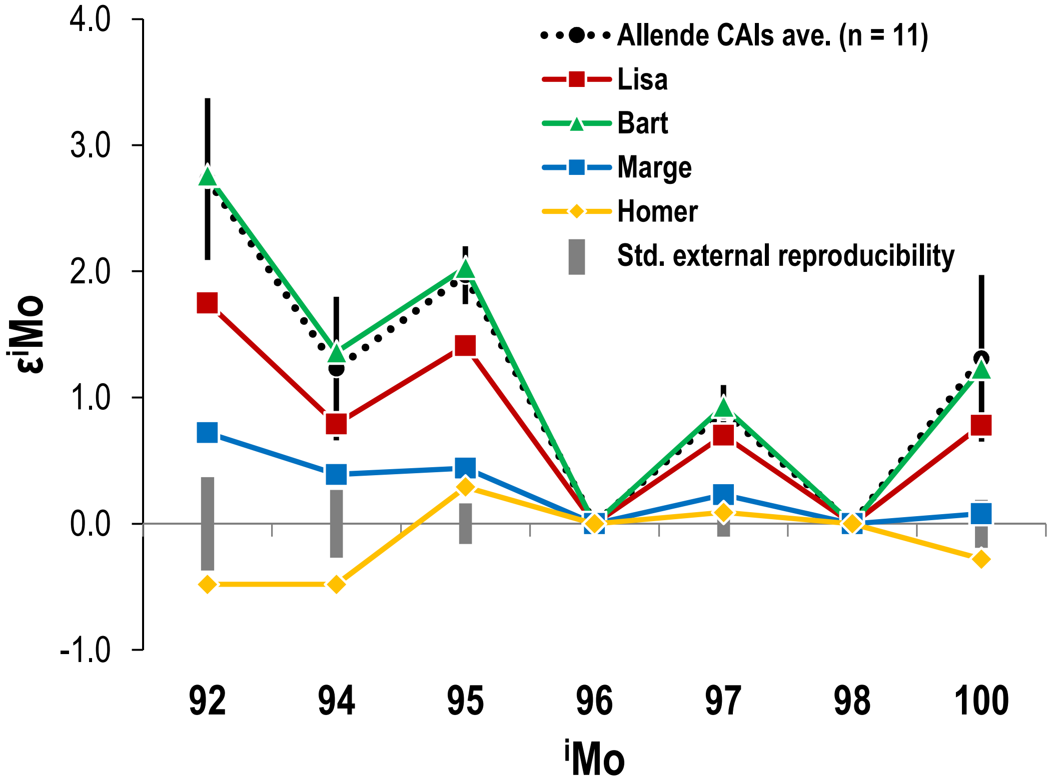

Figure 8. The Mo isotopic compositions of the CAIs analyzed in this study along with the average values for coarse-grained Allende CAIs (data from Burkhardt et al., 2011; Brennecka et al., 2013). Solid grey bars in the plot represents the external uncertainty as defined by the 2SD of the terrestrial rock standard BHVO-2 at the Institut für Planetologie. For clarity purposes, only the uncertainty from the Allende CAIs average values is shown (black error bars).

Table 3. The Mo isotopic compositions of the standards and samples.

	Volts					Normalized to		
Sample	^{96}Mo	ε^{92}Mo	ε^{94}Mo	ε^{95}Mo	ε^{97}Mo	**^{98}Mo/^{96}Mo**	ε^{100}Mo	N
Bart	1.97	2.76	1.36	2.03	0.93	**1.45317**	1.23	6
95% C.I.		0.27	0.17	0.08	0.08		0.12	
Lisa	1.58	1.75	0.79	1.41	0.70	**1.45317**	0.78	3
Marge	1.49	0.72	0.39	0.44	0.23	**1.45317**	0.08	1
Homer	1.44	-0.48	-0.48	0.29	0.09	**1.45317**	-0.28	1
External Reproducibility		0.38	0.27	0.16	0.10	**1.45317**	0.18	
Allende CAIs*		2.73	1.23	1.97	0.89	**1.45317**	1.31	
2SD		0.64	0.57	0.23	0.21		0.66	

*See EA for details on the Allende CAIs calculation

3.2.3 Ba isotopic compositions

The Ba isotopic composition of the samples and standards are provided in Fig. 9 and Table 4 and are given relative to the SRM 3104a standard. Barium has seven isotopes and two (^{134}Ba and ^{136}Ba) are used for internal normalization of the data. The 2SD of the standard during the measurement campaign was 1.9 for ε^{130}Ba, 1.1 for ε^{132}Ba, 0.11 for ε^{135}Ba, 0.10 for ε^{137}Ba, and 0.14 for ε^{138}Ba. Previous work has shown that ^{138}Ba can be affected by the decay of ^{138}La (Brennecka et al., 2013), and thus our reported ε^{138}Ba data are corrected for these affects which were less than 0.1 ε-units in all samples. In this study, no isotopic anomalies are observed outside analytical uncertainty for ε^{130}Ba, ε^{132}Ba, ε^{137}Ba, and ε^{138}Ba. Bart and Lisa have resolved ε^{135}Ba anomalies of 0.40 and 0.41, respectively, and these results are in agreement with most Allende CAIs (Harper et al., 1992; Brennecka et al., 2013; Bermingham et al., 2014). Homer and Marge have ε^{135}Ba of 0.11 and 0.10, respectively, which are within analytical uncertainty of the terrestrial standard.

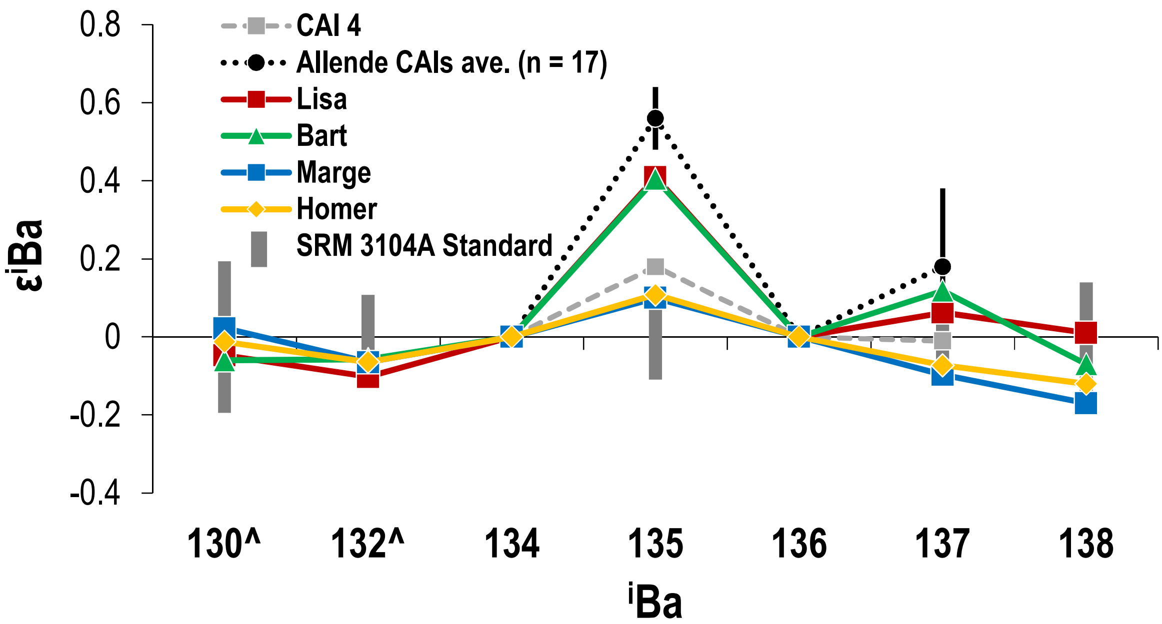

Figure 9. The Ba isotopic compositions of the CAIs analyzed in this study along with the Allende CAIs average value (data from Harper et al., 1992; Brennecka et al., 2013; Bermingham et al., 2014) and CAI 4 from Allende (Bermingham et al., 2014). The uncertainty on the standard (shown as a solid grey bar) in the plots represents the 2SD of the standard during the measurement campaign. For clarity purposes, only the uncertainty from the Allende CAIs average value is shown (black error bars). Not all literature data are reported for both ^{130}Ba and ^{132}Ba so they are not included in the figure, nor is ^{138}Ba due to possible variability caused by unknown radiogenic ingrowth from ^{138}La.

^Denotes isotopic data is divided by 10 to fit on the same scale.

Table 4. The Ba isotopic ratios and La/Ba of the standards and samples.

Sample	Ratios	~µg Ba Loaded	Volts ^{138}Ba	^{130}Ba/^{136}Ba	^{132}Ba/^{136}Bato	Normalized ^{134}Ba/^{136}Ba	^{135}Ba/^{136}Ba	^{137}Ba/^{136}Ba	^{138}Ba/^{136}Ba corr.	^{139}La/^{136}Ba	^{140}Ce/^{136}Ba	Pre Chm La/Ba	ε^{135}Ba	ε^{137}Ba
Bart Ave.	600	0.3	12.7	0.013486	0.012903	**0.3078**	0.839379	1.429032	9.128664	0.000001	0.000000	0.32	**0.40**	**0.12**
Homer Ave.	600	1	13.3	0.013486	0.012903	**0.3078**	0.839354	1.429005	9.128616	0.000000	0.000001	0.01	**0.11**	**-0.07**
Marge Ave.	600	1	13.5	0.013487	0.012903	**0.3078**	0.839353	1.429002	9.128564	0.000001	0.000000	0.02	**0.10**	**-0.10**
Lisa Ave.	800	0.8	12.7	0.013486	0.012902	**0.3078**	0.839379	1.429024	9.128730	0.000001	0.000000	0.07	**0.41**	**0.06**
SRM 3104a														
Ave.	1400	2	12.1	0.013487	0.012904	**0.3078**	0.839345	1.429015	9.128723	0.000001	0.000000		**0.00**	**0.00**
2SD				0.000003	0.000001		0.000009	0.000014	0.000125	0.000003	0.000002		**0.11**	**0.10**
Allende CAIs*													**0.56**	**0.18**
2SD													**0.08**	**0.20**

*See EA for details on the Allende CAIs calculation

3.2.4 Nd isotopic compositions

The Nd isotopic compositions of the samples and standards are presented in Fig. 10 and Table 5, and are given relative to the JNdi standard. Data for ^{142}Nd and ^{143}Nd are not included in the figure due to radiogenic ingrowth from ^{146}Sm and ^{147}Sm, respectively. The long-term external reproducibility of the JNdi standard is 0.08 for ε^{145}Nd, 0.12 for ε^{148}Nd, and 0.22 for ε^{150}Nd. For ε^{145}Nd and ε^{148}Nd, all CAIs of this study show resolved nucleosynthetic anomalies of approximately -0.2 and -0.3 ε-units, respectively, in agreement with Allende CAI Nd isotopic data (Brennecka et al., 2013; Burkhardt et al., 2016). For ε^{150}Nd, Bart, Marge, and Lisa show a uniform depletion of approximately -0.7 ε, also in agreement with literature data (Brennecka et al., 2013; Burkhardt et al., 2016). Homer has a ε^{150}Nd depletion of -0.2 ε, which is within analytical uncertainty to both the terrestrial standard and the average Allende CAI ε^{150}Nd value.

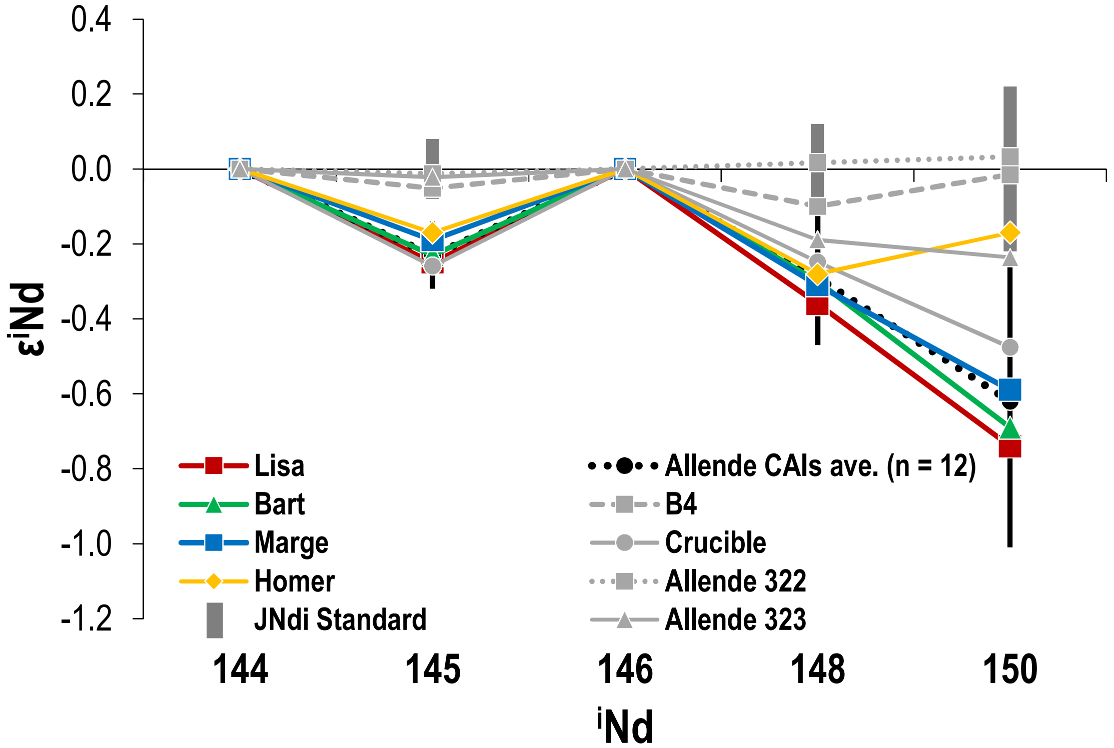

Figure 10. The Nd isotopic compositions of the CAIs analyzed in this study along with the average Nd value for Allende CAIs (Brennecka et al., 2013; Burkhardt et al., 2016) and literature data (Bouvier and Boyet, 2016). The long-term external reproducibility of the JNdi standard is shown as the solid grey bars in the plot. For clarity purposes, only the uncertainty from the average Nd value for Allende CAIs is provided in the figure (black errors

bars). The data, shown in grey, from Bouvier and Boyet (2016) is the bulk CAI measurements where the ^{145}Nd and ^{148}Nd data are the calculated average from line 1 and line 2 in the online supplementary material. The ^{150}Nd data are from line 1 of the same study. The CAI data shown for 'Crucible' is the calculated average of the two analyses of that sample.

Table 5. The Nd isotopic ratios of the standards and samples. The Nd isotopic measurements took place in two different measurement sessions, which are divided in the table.

Sample	Total ratios	~ng Nd Loaded	Volts ^{144}Nd	^{142}Nd/^{144}Nd	^{143}Nd/^{144}Nd	Normalized to ^{146}Nd/^{144}Nd	^{145}Nd/^{144}Nd	^{148}Nd/^{144}Nd	^{150}Nd/^{144}Nd	^{140}Ce/^{144}Nd	^{149}Sm/^{144}Nd	ε^{145}Nd	ε^{148}Nd	ε^{150}Nd
Bart	1080	800	5.4	1.141851	0.512943	**0.7219**	0.348395	0.241571	0.236437	0.000107	0.000001	**-0.23**	**-0.30**	**-0.69**
Marge	1080	900	5.2	1.141853	0.512288	**0.7219**	0.348396	0.241571	0.236440	0.000520	0.000001	**-0.19**	**-0.31**	**-0.59**
Lisa	540	500	4.8	1.141836	0.512640	**0.7219**	0.348394	0.241570	0.236436	0.000081	0.000001	**-0.25**	**-0.36**	**-0.74**
JNdi Ave.	2700	500	4.4	1.141842	0.512100	**0.7219**	0.348403	0.241578	0.236454	0.000001	0.000003			
Homer	540	200	4.4	1.141795	0.512682	**0.7219**	0.348407	0.241576	0.236458	0.000088	0.000025	**-0.17**	**-0.28**	**-0.17**
JNdi Ave.	2700	500		1.141835	0.512110	**0.7219**	0.348413	0.241583	0.236462					
External Reproducibility												**0.08**	**0.12**	**0.22**
Allende CAIs*												**-0.23**	**-0.29**	**-0.62**
2SD												**0.09**	**0.18**	**0.39**

*See EA for details on the Allende CAIs calculation

3.2.5 Sm isotopic compositions

Samarium has seven stable isotopes and two (^{147}Sm and ^{152}Sm) are used for internal normalization. The Sm isotopic compositions of the samples are given as ε-values relative to the Ames Sm standard and are presented in Fig. 11 and Table 6 where the ε^{149}Sm and ε^{150}Sm values are corrected for neutron capture effects (see section 4.1.2 for details about this correction). The long-term external reproducibility of the standard was 0.61 for ε^{144}Sm, 0.19 for ε^{148}Sm, 0.15 for ε^{149}Sm, 0.11 for ε^{150}Sm, and 0.11 for ε^{154}Sm. All samples of this study show relative deficits in ε^{144}Sm and ε^{154}Sm around -2.7 and -0.2, respectively. Homer has a slightly larger depletion in ε^{144}Sm of -3.3 but this is within analytical uncertainty to the other CAIs. All samples show relative excesses in ε^{148}Sm and ε^{150}Sm of approximately 0.5. After neutron capture effects are taken into account, all the Sm isotopic data of this study are in excellent agreement with literature data (Brennecka et al., 2013; Burkhardt et al., 2016; Bouvier and Boyet, 2016). Shown in the Fig. 11 insert is the uncorrected ε^{149}Sm and ε^{150}Sm isotopic compositions of the CAIs. A depletion in ε^{149}Sm is coupled with a predictable excess in ε^{150}Sm as demonstrated most profoundly by Lisa. In contrast, no neutron capture is observed for Bart or Homer.

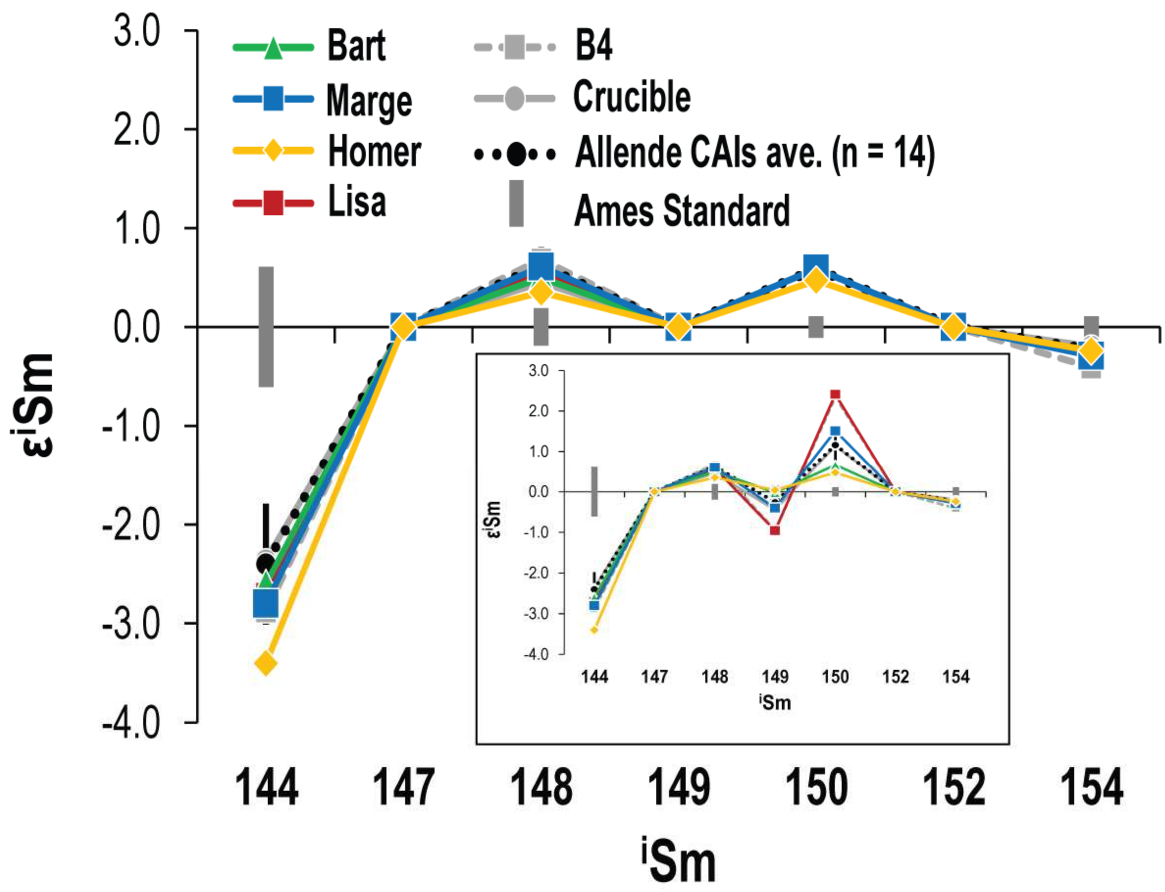

Figure 11. The Sm isotopic compositions of the four CAIs analyzed in this study along with the average Sm value for Allende CAIs (Brennecka et al., 2013; Burkhardt et al., 2016; Bouvier and Boyet, 2016) and two CAIs from desert meteorites (Bouvier and Boyet, 2016). The ε^{149}Sm and ε^{150}Sm values in the large figure have been corrected for neutron capture effects. The uncertainty on the Ames standard (shown as grey bars for each isotope) in the plot represents the long-term external reproducibility (2SD) of that standard. For clarity purposes, only the uncertainty from the average Sm value for Allende CAIs is provided in the figure (black error bars). The data from Bouvier and Boyet (2016) is the bulk CAI measurement. The smaller insert shows Sm isotopic compositions with neutron capture effects where a depletion in ε^{149}Sm is coupled with a predictable excess in ε^{150}Sm.

Table 6. The Sm isotopic ratios of the standards and samples.

Sample	Total ratios	~ng Sm Loaded	Volts ^{144}Sm	^{144}Sm/^{152}Sm	^{148}Sm/^{152}Sm	Normalized to ^{147}Sm/^{152}Sm	^{149}Sm/^{152}Sm meas.	^{150}Sm/^{152}Sm meas.	^{150}Sm/^{152}Sm (nucleosynthetic)	^{154}Sm/^{152}Sm	^{146}Nd/^{152}Sm	^{155}Gd/^{152}Sm	**ε^{144}Sm**	**ε^{148}Sm**	**ε^{150}Sm (nucleosynthetic)**	**ε^{154}Sm**
Bart	200	300	1.71	0.114948	0.420457	**0.56081**	0.516848	0.276009	0.276009	0.850763	0.000378	0.000087	**-2.57**	**0.50**	**0.66 ± 0.19**	**-0.27**
Homer	300	125	1.16	0.114939	0.420451	**0.56081**	0.516851	0.276004	0.276004	0.850765	0.000423	0.000070	**-3.36**	**0.35**	**0.47 ± 0.19**	**-0.24**
Marge	300	275	1.90	0.114946	0.420462	**0.56081**	0.516828	0.276032	0.276006	0.850761	0.000325	0.000070	**-2.76**	**0.61**	**0.56 ± 0.19**	**-0.29**
Lisa	300	150	1.30	0.114946	0.420461	**0.56081**	0.516799	0.276057	0.276006	0.850763	0.000484	0.000107	**-2.74**	**0.58**	**0.56 ± 0.19**	**-0.27**
AMES Ave.	2100		1.57	0.114978	0.420436	**0.56081**	0.516849	0.275991		0.850786	0.000077	0.000004				
2SD													**0.61**	**0.19**	**0.11**	**0.11**
Allende CAIs*													**-2.4**	**0.62**	**0.56 ± 0.19**	**-0.23**
2SD													**0.4**	**0.17**		**0.25**

*See EA for details on the Allende CAIs calculation

4. DISCUSSION

4.1 Sources of isotopic composition alteration

In order to evaluate if CAIs from CK chondrites are different from CV CAIs, the original isotopic compositions must be deduced from the measured compositions which can be altered after CAIs formed. Thus, this alteration can result in measured isotopic compositions that are not truly representative of the original isotopic composition of the inclusion or the CAI-forming region. Previous isotopic analyses of Sr, Mo, Ba, Nd, and Sm have focused on CAIs from the Allende CV3.6 meteorite which, although a fall, is known to have experienced parent body alteration. Nevertheless, CAI samples from Allende show essentially uniform isotope anomalies for most lithophile elements, suggesting that parent body alteration did not significantly affect the isotopic compositions of these elements. However, the samples used in this study are all meteorite finds from Northwest Africa that have likely experienced some degree of terrestrial weathering that must be taken into account (Stelzner et al., 1999). Additionally, secondary thermal neutron capture reactions have modified the isotopic composition of some elements and therefore must be considered for isotopes that have large neutron capture cross sections.

4.1.1 Terrestrial weathering of desert meteorites

The effects of hot-desert weathering on various meteorites have been examined, and it was found that Pb, Ba, and Sr are the most sensitive indicators of such processes (Stelzner et al., 1999; Barrat et al., 2003). Therefore, an increase in Pb, Ba, or Sr concentrations is a simple indicator to evaluate whether a sample has been affected by terrestrial weathering. The observation that, compared to falls, Saharan finds often have elevated Ba and Sr concentrations due to the formation of secondary carbonates and sulfates within fractures of the samples (e.g., Stelzner et al., 1999; Barrat et al., 2003) supports this contention. Additionally, Mo is easily dissolved during weathering in oxidizing conditions and hence selectively mobilized in water (Anbar, 2004). The effects of terrestrial weathering on the REE concentrations is variable as enrichment of the light REEs is observed in shergottites while REE concentrations in eucrites do not show significant modifications (Crozaz et al., 2003). The latter is consistent with the REEs being less soluble and therefore not easily mobilized during weathering. Nonetheless, the effects of hot-desert weathering must be considered for all investigated elements of this study.

Abnormally high abundances of Sr, Mo, and Ba in the CAIs may indicate these elements are contaminated by terrestrial alteration. Note that addition of relatively small amounts of Mo and Ba will have only minor effects on the original isotopic composition of the CAI because the isotopic composition of the contaminant is not significantly different from the unaltered CAI. As a consequence the effects of terrestrial weathering on these isotopic systems may be difficult to identify. However, contamination of Sr in the desert will change the $^{87}Sr/^{86}Sr$ dramatically because the Sr isotopic composition of desert contaminants is vastly different from the Sr isotopic composition of most CAIs. Therefore, a correlation between $^{87}Sr/^{86}Sr$ and other isotopic ratios affected primarily by nucleosynthesis is a clear indication for the addition of terrestrial Sr. Such correlations are presented in Fig. 12a/b/c where $\varepsilon^{84}Sr$, $\varepsilon^{92}Mo$, and $\varepsilon^{135}Ba$ are plotted against $^{87}Sr/^{86}Sr$ for the CAIs. This figure illustrates a trend of increasing radiogenic $^{87}Sr/^{86}Sr$ with decreasing magnitude of stable isotope anomaly. In all three plots, Homer and Marge have the highest $^{87}Sr/^{86}Sr$ values and generally the lowest (if any) nucleosynthetic anomalies. A simple mixing model with one endmember being CAI composition and the other being Western Sahara desert dust composition (Moreno et al., 2006) was used to generate mixing curves in Fig. 12. These curves represent two different desert contaminant compositions ($^{87}Sr/^{86}Sr = 0.7095$ and $^{87}Sr/^{86}Sr = 0.7115$) and mix to the extremes of the average ± 2SD for Allende CAIs (average

Allende CAI data provided in Table EA4). The measured CAI data fall within the model ranges supporting the hypothesis that Homer and Marge were significantly affected by terrestrial contamination for Sr, Mo, and Ba. This is consistent with petrographic examination of Marge which demonstrates the presence of calcites and quartz in cracks, both of which are typical secondary terrestrial contaminants. Therefore, Homer and Marge most likely experienced the addition of terrestrial Sr, Mo, and Ba that shifts the original Sr, Mo, and Ba isotopic compositions toward terrestrial values, thus decreasing the magnitudes of the original anomalies. Therefore, these two CAIs cannot be used to evaluate the nucleosynthetic Sr, Mo, and Ba compositions of the CAI-forming region.

In contrast to Marge and Homer, Lisa and Bart have no clear petrologic evidence for terrestrial weathering, have low $^{87}Sr/^{86}Sr$ values near the Solar System initial value, and have nucleosynthetic anomalies that are in agreement with average Allende CAIs values for Sr, Mo, and Ba. Although there is the potential for the REE isotopic compositions to also be affected by terrestrial weathering, all CAIs of this study show uniform Nd and Sm nucleosynthetic anomalies (Figs. 10 & 11) in comparison with each other and Allende CAIs (Brennecka et al., 2013; Burkhardt et al., 2016; Bouvier and Boyet, 2016). Therefore, it is unlikely that the REE isotopic compositions were significantly affected by terrestrial weathering.

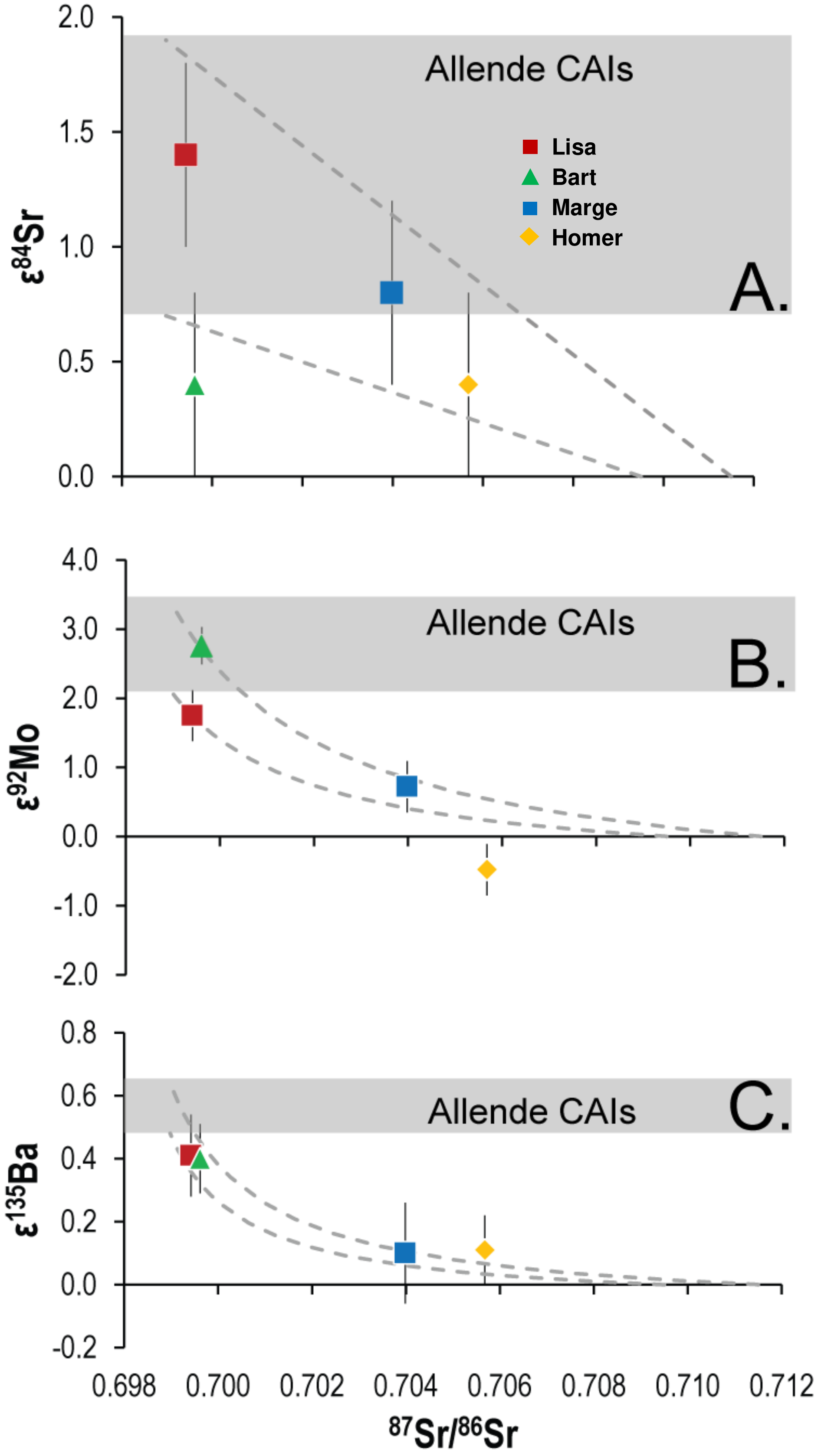
Allende CAIs
Lisa
Bart
Marge
Homer
A.
B.
C.
ε84Sr
ε92Mo
ε135Ba
2.0
1.5
1.0
0.5
0.0
4.0
3.0
2.0
1.0
0.0
-1.0
-2.0
0.8
0.6
0.4
0.2
0.0
-0.2
0.698
0.700
0.702
0.704
0.706
0.708
0.710
0.712
87Sr/86Sr

561

Figure 12. (A) Plot of ε^{84}Sr versus ^{87}Sr/^{86}Sr for the CAI samples of this study. Generally, the samples with higher ^{87}Sr/^{86}Sr have lower ε^{84}Sr. This is consistent with the addition of terrestrial Sr to the samples resulting in higher ^{87}Sr/^{86}Sr and thus a dilution of the original ε^{84}Sr. Modeled mixing curves are represented by dashed grey lines. The 2SD of the average Allende CAIs ε^{84}Sr is shown as the grey box. (B) Same as (A) but ε^{92}Mo versus ^{87}Sr/^{86}Sr. (C) Same as (A) but ε^{135}Ba versus ^{87}Sr/^{86}Sr. (Allende average CAI data from Harper et al., 1992; Moynier et al., 2012; Hans et al., 2013; Burkhardt et al., 2011; Brennecka et al., 2013; Bermingham et al., 2014)

4.1.2 Neutron capture in CAIs

Accounting for neutron capture in Sm isotope systematics

Another source for secondary isotopic variations can occur within the Sm isotope system and is caused by the capture of thermal neutrons. The isotope ^{149}Sm has an exceptionally large thermal neutron capture cross section (~40,000 barns), indicating that it is far more likely to capture a secondary neutron produced by galactic cosmic rays penetrating meteorite parent bodies than other isotopes. The extent of neutron capture effects are controlled by the dose of cosmic rays and the chemical composition of the irradiated material. As such, these effects are generally only thought to be high enough to cause isotopic shifts within several meters below the surface. Capture of thermal neutrons by ^{149}Sm results in depletions of ^{149}Sm that correlate with predictable excesses of ^{150}Sm. This is a well-known effect that has been reported for samples such as lunar rocks, aubrites, and even in many chondritic meteorite parent bodies (e.g., Russ et al., 1971; Hidaka et al., 1999, 2000a, 2000b, 2012; Carlson et al., 2007; Burkhardt et al., 2016). However, evidence for such effects is minimal in CAIs (Bouvier and Boyet, 2016).

Previous studies examining CAIs have considered neutron capture on ^{149}Sm, producing ^{150}Sm, but were unable to identify the effects of this process due to limited spread of the ^{149}Sm and ^{150}Sm in the sample suites analyzed (Brennecka et al., 2013; Bouvier and Boyet, 2016). The data presented here clearly demonstrate evidence for neutron capture (Fig. 13). The insert to Fig. 13 illustrates that the CAIs of this study fall on a theoretical neutron capture line indicative of neutron capture in these samples. Note the theoretical neutron capture line has a slope of -1 in ^{149}Sm/^{152}Sm versus ^{150}Sm/^{152}Sm space which translates to a slope of -1.87 when plotted in epsilon space using the Ames standard measured during this investigation. From Fig. 13 it is apparent that the CAIs analyzed here, as well as those CAIs reported in the literature, plot along a linear trend parallel to the theoretical neutron capture line that passes though the Ames Sm standard and bulk Earth values. This offset is an expression of the nucleosynthetic effects on Sm in the CAIs. The linearity and data range of the CAIs in Fig. 13 demonstrates that the CAIs have the same Sm isotopic compositions but experienced different amounts of thermal neutron irradiation. It is not surprising that Lisa and B4 (Bouvier and Boyet, 2016), which are both CAIs derived from NWA 6991, have nearly identical ε^{149}Sm and ε^{150}Sm compositions (Fig. 13) indicating that they have experienced similar thermal neutron irradiation histories. However, Bart and Homer have ε^{149}Sm compositions that are within uncertainty to the terrestrial standard values, reflecting the fact that these two CAIs did not experience significant thermal neutron irradiation.

Quantifying the nucleosynthetic Sm isotopic signatures in CAIs

After the consideration of neutron capture in CAIs, the nucleosynthetic component in the ε^{149}Sm and ε^{150}Sm can be quantified. The observation that CAIs Bart and Homer have terrestrial ε^{149}Sm compositions indicate that they are not affected by neutron capture, and thus their measured excesses in ε^{150}Sm are solely due to nucleosynthetic processes. This provides a ε^{150}Sm baseline value for CAIs that are unaffected by neutron capture. In contrast, Lisa has an ε^{149}Sm of ~ -1 and a corresponding excess in ε^{150}Sm reflecting both a neutron capture component (ε^{150}Sm ~ 1.8) and a nucleosynthetic component (ε^{150}Sm ~ 0.56 ± 0.19). Therefore, the coupled Sm isotopic compositions of irradiated and non-irradiated CAIs demonstrate that the source of all CAIs measured thus far has a ε^{149}Sm of ~0 and ε^{150}Sm of ~0.56 ± 0.19 that is attributable to differences in nucleosynthetic processes responsible for the production of the Sm. Although neutron capture can potentially alter the original isotopic composition of CAIs, the neutron capture cross sections of the other isotopes in this study (e.g., Sr, Mo, Ba, and Nd) are approximately 200 times less than ^{149}Sm making the effects of neutron capture negligible at the current level of precision.

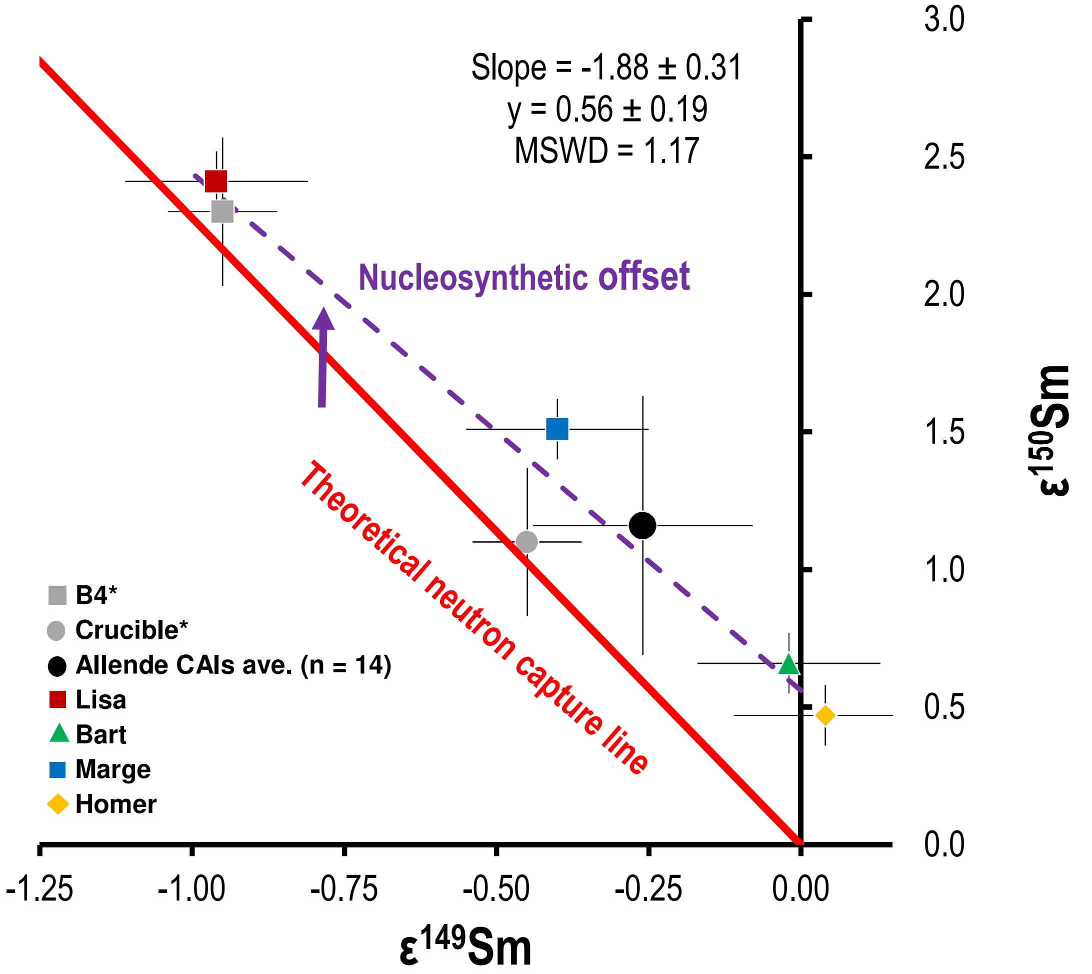

Figure 13. Evidence for neutron capture in CAIs of this study along with two non-Allende CAIs (Bouvier and Boyet, 2016) and the average Allende CAI value (Brennecka et al., 2013; Burkhardt et al., 2016; Bouvier and Boyet, 2016). The solid red line on the plot represents the theoretical neutron capture line (slope of -1.87). The purple dashed line is a regression calculated by *Isoplot* with the slope and y-intercept shown in the plot (uncertainties on the slope and intercept are 95% confidence intervals). The samples in this study plot on a parallel line slightly above the theoretical line. The offset, indicated by the purple arrow, between the lines is due to nucleosynthetic anomalies

present in CAIs. The y-intercept is the nucleosynthetic contribution on ε^{150}Sm in CAIs. Error bars for the samples represent the long-term 2SD of the terrestrial standard from each individual study except for the average Allende CAIs in which the error bars represent the 2SD of the average values.
*Denotes non-Allende CAI data from Bouvier and Boyet (2016).

Neutron fluence estimation in CAIs

The measured neutron capture effects in the CAI samples can be used to calculate the neutron fluence they experienced. This calculation utilizes isotope ratios so all the ε-values from the other studies (Brennecka et al., 2013; Burkhardt et al., 2016; Bouvier and Boyet, 2016) were transformed into isotope ratios using the Ames standard value from Table 6. However, before this calculation can be completed it is necessary to subtract out the nucleosynthetic component in the CAIs for the ^{150}Sm/^{152}Sm and this step utilized the y-intercept in Fig. 13 (y = 0.56 ε). The neutron fluences (Ψ) are shown in Table 7 for each CAI which were estimated using the following equation (Hidaka et al., 2012).

$$\Psi = \frac{\left({}^{150}\mathrm{Sm}/{}^{149}\mathrm{Sm}\right)_{sample} - \left({}^{150}\mathrm{Sm}/{}^{149}\mathrm{Sm}\right)_{Std}}{\left({}^{150}\mathrm{Sm}/{}^{149}\mathrm{Sm}\right)_{STD2} - \left({}^{150}\mathrm{Sm}/{}^{149}\mathrm{Sm}\right)_{Std}} \times \frac{(\sigma)_{STD2}}{(\sigma)_{sample}} \times (5.94 \times 10^{15}) \qquad (1)$$

In equation 1, STD2 is ‘irrad STD1’ (Hidaka et al., 1995) which has a known neutron fluence, σ is the thermal neutron capture cross section of STD2 and each sample, and $(^{150}\mathrm{Sm}/^{149}\mathrm{Sm})_{\mathrm{Std}}$ is the Ames standard of this study (provided in Table 7). The measured ^{149}Sm/^{152}Sm and corrected ^{150}Sm/^{152}Sm of the CAIs were used to generate $(^{150}\mathrm{Sm}/^{149}\mathrm{Sm})_{\mathrm{sample}}$ as shown in Table 7 and these values were used in equation 1 to estimate the neutron fluence for each CAI.

Comparing neutron fluences between individual CAIs to bulk chondrites can provide insights into the relationship between CV and CK chondrites. The neutron fluences for the CAIs presented in this study range from 8.40×10^{13} to 2.11×10^{15} n/cm^2 and are consistent with previous ranges, 0.93 – 4.41 $\times10^{15}$ n/cm^2, for chondrites (e.g. Hidaka et al., 2000b). The Allende CAIs span a range of 4.11×10^{14} – 1.09 $\times10^{15}$ n/cm^2 which is similar to the bulk Allende values of 1.44×10^{15} n/cm^2 and 2.17×10^{15} n/cm^2 (Hidaka et al., 2000b). When galactic cosmic rays penetrate relatively large bodies (e.g., meteorites, parent bodies), high energy neutrons are slowed down to thermal energies through cascades of nuclear reactions resulting in thermalized neutrons. Thus, the neutron capture reactions observed here in the CAIs must have occurred after the CAIs were incorporated in their parent bodies or perhaps more likely, after the meteorites were broken apart from their parent bodies. If the CAIs from CK and CV chondrites are derived from a single parent body (as certain models suggest e.g., Elkins-Tanton et al., 2011), the different neutron fluences observed for individual CAIs could be indicative of various depths of burial. Alternatively, if CV and CK chondrites are from different parent bodies (e.g., Dunn et al., 2016; Yin et al., 2017), then the various neutron fluences may reflect the different irradiation histories and/or depths of burial for these particular samples. Regardless of when the irradiation occurred, the CV CAIs must have been located within a few meters of the surface of the body and the CK CAIs were exposed to fewer thermalized neutrons.

Table 7. Estimation of neutron fluence in CAIs.

Samples	^{150}Sm/^{149}Sm	Ψ (n/cm^2)
Bart (CK3)	0.533993	8.40E+13

Homer (CK3)	0.533980	0.00E+00
Marge (CV3)	0.534059	1.02E+15
Lisa[a] (CV3)	0.534137	2.11E+15
B4[a,b] (CV3)	0.534132	2.04E+15
Crucible[b] (CV3)	0.534042	7.65E+14
Allende CAIs[c] (CV3)	0.534016 - 0.534065	4.11E+14 - 1.09E+15
Ames Standard	0.533987	0.00E+00

Neutron fluence calculations were done following Hidaka et al. (2012).
[a] Indicates a CAI from NWA 6991
[b] Data from Bouvier and Boyet, 2016
[c] Data from Brennecka et al., 2013; Burkhardt et al., 2016; Bouvier and Boyet, 2016

4.2 Probing the original isotopic composition of the CV/CK CAI-forming region

Sr, Mo, Ba, Nd, and Sm isotopes in CAIs

The isotopic composition of the CV CAI-forming region is characterized—using mostly Allende CAIs—by excesses in ε^{84}Sr, ε^{135}Ba, ε^{137}Ba, ε^{92}Mo, ε^{94}Mo, ε^{95}Mo, ε^{97}Mo, ε^{100}Mo, ε^{148}Sm, and ε^{150}Sm along with depletions in ε^{145}Nd, ε^{148}Nd, ε^{150}Nd ε^{144}Sm, and ε^{154}Sm. However, a discussion of each elemental system with the addition of non-Allende CV and CK CAI data allows for the direct characterization of the region where these CAIs formed.

The Sr isotopic compositions of (n=17) Allende CAIs reported in three different studies (Moynier et al., 2012; Hans et al., 2013; Brennecka et al., 2013) yield an average ε^{84}Sr of 1.3 ± 0.6 (2SD, Table EA4), although an ε^{84}Sr range of 0.30 – 2.87 for Allende CAIs has been reported demonstrating variability in ε^{84}Sr (Charlier et al., 2017). Despite derivation from a desert meteorite that could have experienced terrestrial weathering, the Sr isotopic composition of Lisa (ε^{84}Sr = 1.4) is in good agreement with previous results, including Allende and non-Allende CAIs (Fig. 7; Moynier et al., 2012; Hans et al., 2013; Paton et al., 2013; Brennecka et al., 2013). In contrast, Bart has an ε^{84}Sr anomaly of 0.4, which is within analytical uncertainty of the terrestrial standard and the Allende CAIs average value. However, Bart has clearly experienced metamorphism on the parent body as indicated by two generations of plagioclase. Considering that anorthitic plagioclase incorporates large amounts of Sr, this low ε^{84}Sr value most likely reflects the addition of parent body Sr that diluted the original Sr composition. Regardless, most CAIs (Allende and non-Allende) cluster around a mean ε^{84}Sr of approximately 1.3 (Fig. 7) that represents the original Sr isotopic composition in the CAI-forming region.

The average of 17 Allende CAIs have Ba isotopic compositions of 0.56 ± 0.08 for ε^{135}Ba and 0.18 ± 0.20 for ε^{137}Ba (2SD, Table EA4; Harper et al., 1992; Brennecka et al., 2013; Bermingham et al., 2014) demonstrating isotopic homogeneity, although one Allende CAI was reported to have a small enrichment in ε^{135}Ba and slight deficit in ε^{137}Ba that are indistinguishable from terrestrial standards (see Fig. 9; Bermingham et al., 2014). However, because no Ba concentration, REE pattern, or Sr isotope ratios were reported for this CAI, it is not clear whether this CAI reflects Ba isotopic heterogeneity in the CAI-forming region, or perhaps more likely, reflects contamination of Ba from the environment. From this study, Bart and Lisa both have excesses that are clearly distinct from terrestrial standards in ε^{135}Ba (Table 4) and these inclusions hint at enrichments in ε^{137}Ba as well, but these are not clearly resolved. Lisa, from a CV meteorite, and Bart, from a CK meteorite, both have a similar Ba isotopic compositions to Allende CAIs indicating they formed in the same isotopic reservoir.

Contrary to many other isotopic systems, previous work has shown isotopic variability exists between fine- and coarse-grained CAIs for Mo (Burkhardt et al., 2011; Brennecka et al., 2017). Nevertheless all coarse-grained CAIs measured thus far appear have uniform Mo isotope patterns (Yin et al., 2002; Becker and Walker, 2003; Burkhardt et al., 2011; Brennecka et al., 2013, 2017) and since only coarse-grained CAIs were analyzed here, these types of CAIs will be the focus of this discussion. The average Mo isotopic composition of coarse-grained Allende CAIs exhibits positive excesses relative to terrestrial values in all isotopes of Mo (ε^{92}Mo, ε^{94}Mo, ε^{95}Mo, ε^{97}Mo, and ε^{100}Mo) and shows a distinct 'kink' on ε^{94}Mo (Becker and Walker, 2003; Burkhardt et al., 2011; Brennecka et al., 2013). Bart and Lisa have well defined excesses relative to terrestrial standards in ε^{92}Mo, ε^{94}Mo, ε^{95}Mo, ε^{97}Mo, and ε^{100}Mo with the above-mentioned 'kink' on ε^{94}Mo and are isotopically similar to the majority of coarse-grained Allende CAIs having the characteristic *r*-excess pattern, thus demonstrating derivation from the same isotopic reservoir.

The Nd isotopic compositions of the CV and CK CAIs in this work have depletions in ε^{145}Nd, ε^{148}Nd, and ε^{150}Nd consistent with Allende CAIs (Brennecka et al., 2013; Burkhardt et al., 2016). Although Homer has a smaller depletion in ε^{150}Nd compared to the rest of the CAIs of this study, the excellent agreement in the ε^{145}Nd and ε^{148}Nd compositions (that is consistent with a modelled *r*-process deficit in Nd) of Homer with other CAIs provides evidence that the ε^{150}Nd may simply represent a measurement at the edge of analytical uncertainty. The Nd data of this study demonstrates that CAIs with varying mineralogy from CV and CK meteorites formed in a region that was isotopically uniform regarding Nd. In contrast, Bouvier and Boyet (2016) reported three CAIs with Nd isotopic compositions that were indistinguishable from terrestrial standards (Fig. 10), yet the same three CAIs had nucleosynthetic anomalies in their Sm isotopic compositions. It is difficult to explain how CAIs could have terrestrial Nd compositions but anomalous Sm compositions. Regardless, the majority of CAIs measured to this point show remarkably uniform and distinct Nd isotopic compositions.

After correction for neutron capture effects, all CAIs measured to this point from both CV and CK meteorites have nucleosynthetic anomalies in ε^{144}Sm, ε^{148}Sm, ε^{150}Sm, and ε^{154}Sm that are resolved from terrestrial standards yet agree within analytical uncertainty of one another (Fig. 11 literature data from: Brennecka et al., 2013; Burkhardt et al., 2016; Bouvier and Boyet, 2016). This provides strong evidence for an isotopically homogenous CV/CK CAI-forming region.

A large-scale, CAI-forming region?

After the consideration of hot-desert weathering and neutron capture, the Sr, Ba, Nd, and Sm isotopic compositions of the CAIs analyzed from non-Allende CV and CK chondrites are uniform with each other and Allende CAIs, and all are distinct from terrestrial standards. This implies that the region where these objects formed was homogenous for these elements and thus suggests a single isotopic reservoir for CV and CK CAI formation. However, this homogeneity is inconsistent with the observed isotopic differences between fine- and coarse-grained CAIs in the elements Mo and W (Burkhardt et al., 2011, Kruijer et al., 2014; Brennecka et al., 2017), along with slight isotopic variability in Ca, Ti, Cr, Ni, Zr, and Hf (e.g., Birck and Lugmair 1988, Huang et al., 2012; Akram et al., 2013; Mercer et al., 2015; Williams et al. 2016; Peters et al., 2017; Davis et al., 2017). The isotopic variability in these elements could reflect 1) the phases various elements are in during condensation along with their presolar carriers and/or 2) secondary processing such as interaction with nebular gas and/or parent body processing. For example, an integrated isotopic study on CAIs by Brennecka et al. (2017) has demonstrated there is large isotopic variability in the siderophile elements Mo and W and interpreted this to possibly reflect uneven distribution of the presolar carrier(s) of these elements. In comparison, the coarse-grained CAIs of this work are consistent with Mo isotopic compositions measured in previous studies on coarse-grained CV CAIs (Burkhardt et al., 2008; Brennecka et al., 2013, 2017), demonstrating that these types of CAIs from CV and CK meteorites are identical and implying formation in a single nebular region.

Slight isotopic variation in the lithophile elements Ca, Ti, Zr, and Hf reported in CAIs could also reflect the phases these elements condensed in. For example, elements like Ca and Ti are primarily hosted in melilite whereas Zr and Hf are expected to condense in oxides (Lodders, 2003). Therefore, the carriers of Zr and Hf anomalies are likely different than those of Ca and Ti, and it is possible that not all of these carriers were mixed to the same degree. Even so, the variability in Zr and Hf is generally < 1 ε and the majority of CAIs do have uniform Zr and Hf isotopic compositions (Sprung et al., 2010; Akram et al., 2013; Render et al., 2016; Peters et al., 2017). Similarly, Ti isotopic compositions of CAIs generally span a narrow range of excesses that cluster around 1.4 in ε^{46}Ti and 9.5 in ε^{50}Ti (Williams et al., 2016; Davis et al., 2017). Therefore, these data sets do not exclude the possibility of CAI formation in a single nebular region but instead reflect that some presolar carriers were well-mixed but not completely homogenized.

Elements such as Cr and Ni could also have heterogeneously distributed carriers in the CAI-forming region, although the effects of secondary processing could also explain some of the observed isotopic variability. Previous studies reported variability in Cr and Ni isotopes in CAIs (e.g., Birck and Lugmair 1988), however, more recent work on Cr demonstrated that this variability likely reflects partial equilibration of parent body Cr with the CAIs (Trinquier et al., 2009; Mercer et al., 2015). As the Cr concentration ratio of chondrites to CAIs is ~ 10 (with CI chondrites as a proxy for a CAI-free matrix), a small addition of Cr from the matrix to the CAI could significantly alter the CAI isotopic composition (Trinquier et al., 2009; Mercer et al., 2015). Such a scenario could also extend to Ni as previous work has shown the mobility of Ni between chondrules and matrix during aqueous alteration and/or terrestrial weathering (Telus et al., 2016). This exchange would result in Ni isotopic compositions that are not indicative solely of the CAI-forming region, but of a mix between Ni from the CAI region and Ni from the bulk meteorite. Therefore, Cr and Ni heterogeneity in CAIs might reflect secondary processing of individual samples on their parent bodies and/or terrestrial alteration. In any case, these effects need to be carefully considered with regards to the CAI-forming region.

If CV and CK CAIs formed in different nebular regions, we would expect variability in their isotopic compositions, yet, the CAIs Bart and Homer from CK meteorites have isotopic compositions that are similar to CV CAIs, regardless of mineralogy, petrology, REE pattern, or documented alteration. Thus, the isotopic compositions of CAIs from both CV and CK chondrites imply that there existed a largely homogeneous CAI-forming region, at least with respect to the lithophile elements. Such a scenario could imply that CAIs from other chondritic meteorites would have the same isotopic compositions as CV and CK CAIs, however this remains largely untested.

5. Conclusions

(1) In this study and previous work, a variety of CAI types (A, B, related to C, group II and non-group II, fine-grained, coarse-grained) have been analyzed for Sr, Mo, Ba, Nd, and Sm isotope systematics. Regardless of the CAI sample, the vast majority of the analyzed CAIs are indistinguishable from each other within analytical uncertainty but are clearly resolvable from terrestrial values. Nucleosynthetic anomalies observed in CAIs from CK3 meteorites for Mo, Ba, Nd, and Sm are consistent and in good agreement with CAIs from CV3 meteorites (Harper et al., 1992; Burkhardt et al., 2011; Brennecka et al., 2013; Bermingham et al., 2014; Bouvier and Boyet, 2016; Burkhardt et al., 2016). This is evidence that CAIs from CV and CK chondrites formed in the same nebular region that was essentially isotopically homogenous for these elements.

(2) The lesser magnitude (or absent) nucleosynthetic anomalies in the Sr, Mo, and Ba isotopic compositions of two CAIs in this study stems from hot-desert weathering that diluted the original Sr, Mo, and Ba isotopic composition of those inclusions. Therefore, these measured isotopic compositions are not indicative of the CAI-forming region, but instead of the original CAI composition mixed with terrestrial contamination in these elements. Petrographic data and other isotopic data such as $^{87}Sr/^{86}Sr$ ratios can assist in determining if hot-desert weathering has affected samples. However, the isotopic composition of REE elements such as Sm and Nd appear to have not been affected by terrestrial weathering in these samples.

(3) The Sm isotopic composition measured in CAIs here and in previous studies clearly demonstrates that neutron capture effects have altered the Sm isotopic composition of some CAIs. To this point, secondary effects from neutron capture are restricted to CAIs from CV chondrites, whereas CK CAIs show no effects from neutron capture. However, when neutron capture effects are taken into account, all CAIs measured thus far show remarkable isotopic uniformity for Sm systematics.

Acknowledgements

This work was performed under the auspices of the US Department of Energy by Lawrence Livermore National Laboratory under Contract DE-AC52-07NA27344. This work was supported by the National Aeronautics and Space Administration Cosmochemistry grants NNH16AC441 and Laboratory Directed Research and Development grant 17-ERD-001 (L.E.B.), and a Sofja Kovalevskaja Award from the Humboldt Foundation (G.A.B.). Europlanet 2020 RI has received funding from the European Union's Horizon 2020 research and innovation program under grant agreement No 654208. A.B. and S.E. thank the DFG for support within the SFB-TRR 170 "Late Accretion onto Terrestrial Planets" (subproject B5; AB). This is TRR 170 publication No. 43. We thank Nicolas Dauphas for his editorial efforts and two anonymous reviewers for their helpful comments that improved the manuscript. The authors are appreciative of thoughtful discussions with T. Kruijer and thank T. Goral and C. Ramon for assistance with the sample preparation and characterization. Additionally, C. Brennecka is thanked for assistance with writing clarity.

References

Akram W., Schönbächler M., Sprung P., and Vogel N. (2013) Zirconium-hafnium isotope evidence from meteorites for the decoupled synthesis of light and heavy neutron-rich nuclei. *Astrophys. J.* **777**, 169-181.

Amelin Y., Kaltenbach A., Iizuka T., Stirling C.H., Ireland T.R., Petaev M., and Jacobsen S.B. (2010) U-Pb chronology of the Solar System's oldest solids with variable $^{238}U/^{235}U$. *Earth Planet. Sci. Lett.* **300**, 343-350.

Anbar A. (2004) Molybdenum Stable Isotopes: Observations, Interpretations and Directions. Reviews in Mineralogy & Geochemistry **55**, 429-454.

Andreasen R. and Sharma M. (2007) Mixing and Homogenization in the early solar system: clues from Sr, Ba, Nd, and Sm Isotopes in Meteorites. *Astrophys. J.* **665**, 874-883.

Armstrong J. T. (1991) Quantitative elemental analysis of individual microparticles with electron beam instruments. In *Electron probe quantitation* (eds. K. F. J. Heinrich and D. E. Newbury). Plenum Press, New York. pp. 261–315.

Bar-Matthews M., Hutcheon I.D., MacPherson G.J., and Grossman L. (1982) A corundum-rich inclusion in the Murchison carbonaceous chondrite *Geochim. Cosmochim. Acta* **46**, 31-41.

Barrat J.A., Jambon A., Bohn M., Blichert-Toft J., Sautter V., Göpel C., Gillet PH., Boudouma O., and Keller F. (2003) Petrology and geochemistry of the unbrecciated achondrite Northwest Africa 1240 (NWA 1240): An HED parent body impact melt. *Geochim. Cosmochim. Acta* **67**, 3959-3970.

Becker H. and Walker R.J. (2003) Efficient mixing of the solar nebula from uniform Mo isotopic composition of meteorites. *Nature* **425**, 152-155.

Bermingham K.R., Mezger K., Desch S.J., Scherer E.E., and Horstmann M. (2014) Evidence for extinct ^{135}Cs from Ba isotopes in Allende CAIs? *Geochim. Cosmochim. Acta* **133**, 463-478.

Birck J. L. and Lugmair G. W. (1988) Nickel and chromium isotopes in Allende inclusions. *Earth Planet. Sci. Lett.* **90**, 131–143.

Bischoff A. and Palme H. (1987) Composition and mineralogy of refractory metal-rich assemblages from a Ca,Al-rich inclusion in the Allende meteorite. *Geochim. Cosmochim. Acta* **51**, 2733-2748.

Bizzarro M., Baker J. A., and Haack H. (2004) Mg isotope evidence for contemporaneous formation of chondrules and refractory inclusions. *Nature* **431**, 275-278.

Borg L.E., Brennecka G. A., and Symes S. J. K. (2016) Accretion timescale and impact history of Mars deduced from the isotopic systematics of martian meteorites. *Geochim. Cosmochim. Acta* **175**, 150-167.

Bouvier A., Brennecka G.A., and Wadhwa M. (2011) Absolute chronology of the first solids in the solar system. *Workshop on Formation of the First Solids in the Solar System*, #9054.

Bouvier A. and Boyet M. (2016) Primitive Solar System materials and Earth share a common initial ^{142}Nd abundance. *Nature* **537**, 399–402.

Boynton W.V. (1975) Fractionation in the solar nebula: condensation of yttrium and the rare earth elements. *Geochim. Cosmochim. Acta* **39**, 569-584.

Brennecka G.A., Borg L.E., and Wadhwa M. (2013) Evidence for supernova injection into the solar nebula and the decoupling or r-process nucleosynthesis. *Proc. Nat. Acad. Sci.* **110**, 17241-17246.

Brennecka G.A., Burkhardt C., Kruijer T.S., and Kleine T. (2017) Towards understanding the source of nucleosynthetic anomalies in refractory inclusions. *Lunar Planet. Sci.* **48**, #1619.

Burkhardt C. Kleine T., Oberli F., Pack A., Bourdon B., and Wieler R. (2011) Molybdenum isotope anomalies in meteorites: Constraints on solar nebula evolution and origin of the Earth. *Earth Planet. Sci. Lett.* ***312***, 390-400.

Burkhardt C., Borg L.E., Brennecka G.A., Shollenberger Q.R., Dauphas N., and Kleine T. (2016) A nucleosynthetic origin for the Earth's anomalous ^{142}Nd composition. *Nature* **537**, 394-398.

Carlson R.W., Boyet M., and Horan M. (2007) Chondrite barium, neodymium, and samarium isotopic heterogeneity and early Earth differentiation. *Science* **316**, 1175-1178.

Charlier B.L.A., Tissot F.L.H., and Dauphas N. (2017) Strontium stable isotope composition of Allende fine-grained inclusions. *Lunar Planet. Sci.* **48**, #2352.

Connelly J.N., Ulfbeck D.G., Thrane K., Bizzarro M., and Housh T. (2006) A method for purifying Lu and Hf for analyses by MC-ICP-MS using TODGA resin. *Chemical Geology* **233**, 126-136.

Connelly J.N., Bizzarro M., Krot A.N., Nordlund Å., Wielandt D., and Ivanova M.A. (2012) The absolute chronology and thermal processing of solids in the solar protoplanetary disk. *Science* **338**, 651-655.

Crozaz G., Floss C., and Wadhwa M. (2003) Chemical alteration and REE mobilization in meteorites from hot and cold deserts. *Geochim. Cosmochim. Acta* **67**, 4727-4741.

Dauphas N. and Schauble E.A. (2016) Mass fractionation laws, mass-independent effects, and isotopic anomalies. *Annu. Rev. Earth Planet. Sci.* **44**, 709-783.

Davis A.M. and Grossman L. (1979) Condensation and fractionation of rare earths in the solar nebula. *Geochim. Cosmochim. Acta* **43**, 1611-1632.

Davis A. M., Zhang, J., Hu J., Greber N. D., and Dauphas N. (2018) Titanium isotopes and rare earth patterns in CAIs: evidence for thermal processing and gas-dust decoupling in the protoplanetary disk. *Geochim. Cosmochim. Acta* **221**, 275-295.

Dunn T.L., Gross J., Ivanova M.A., Runyon S.E., and Bruck A.M. (2016) Magnetite in the unequilibrated CK chondrites: Implications for metamorphism and new insights into the relationship between the CV and CK chondrites. *MAPS* **51**, 1701-1720.

Elkins-Tanton L.T., Weiss B.P., and Zuber M.T. (2011) Chondrites as samples of differentiated planetesimals. *Earth Planet. Sci. Lett.* **305**, 1-10.

Geiger T. and Bischoff A. (1995) Formation of opaque minerals in CK chondrites. *Planet. Space Sci*. **43**, 485-498.

Hans U., Kleine T., and Bourdon B. (2013) Rb-Sr chronology of volatile depletion in differentiated protoplanets: BABI, ADOR and ALL revisited. *Earth Planet. Sci. Lett.* **374**, 204-214.

Harper C.L., Weismann H., and Nyquist L.E. (1992) The search for ^{135}Cs is the early solar system: Very high precision measurements of barium isotopes in bulk Allende and refractory inclusions. *Meteoritics* **27**, 230-231.

Hidaka H. and Ebihara M. (1995) Determination of the isotopic compositions of samarium and gadolinium by thermal ionization mass spectrometry. *Anal. Chem.* **67**, 1437-1441.

Hidaka H., Ebihara M., and Yoneda S. (1999) High fluences of neutrons determined from Sm and Gd isotopic compositions in aubrites. *Earth Planet. Sci. Lett.* **173**, 41-51.

Hidaka H., Ebihara M., and Yoneda S. (2000a) Neutron capture effects on samarium, europium, and gadolinium in Apollo 15 deep drill-core samples. *MAPS* **35**, 581-589.

Hidaka H., Ebihara M., and Yoneda S. (2000b) Isotopic study of neutron capture effects on Sm and Gd in chondrites. *Earth Planet. Sci. Lett.* **180**, 29-37.

Hidaka H., Kondo T., and Yoneda S. (2012) Heterogeneous isotopic anomalies of Sm and Gd in the Norton county meteorite: evidence for irradiation from the active early sun. *Astrophys. J.* **746**, 132.

Huang S., Farkas J., Yu G., Petaev M.I., and Jacobsen S.B. (2012) Calcium isotopic ratios and rare earth element abundances in refractory inclusions from the Allende CV3 chondrite. *Geochim. Cosmochim. Acta* **77**, 252-265.

Jacobsen B., Yin Q., Moynier F., Amelin Y., Krot A.N., Nagashima K., Hutcheon I.D., and Palme H. (2008) ^{26}Al-^{26}Mg and ^{207}Pb-^{206}Pb systematics of Allende CAIs: Canonical solar initial ^{26}Al/^{27}Al ratio reinstated. *Geochim. Cosmochim. Acta* **272**, 353-364.

Keller L.P., Clark J.C., Lewis C.F., and Moore C.B. (1992) Maralinga, a metamorphosed carbonaceous chondrite found in Australia. *Meteoritics* **27**, 87-91.

Kööp L., Davis A.M., Nakashima D., Park C., Krot A.N., Nagashima K., Tenner T.J., Heck P.R., and Kita N.T. (2016) A link between oxygen, calcium, and titanium isotopes in ^{26}Al-poor hibonite-rich CAIs from Murchison and implications for the heterogeneity of dust reservoirs in the solar nebula. *Geochim. Cosmochim. Acta* **189**, 70-95.

Kruijer T.S., Kleine T., Fischer-Gödde M., Burkhardt C., and Wieler R. (2014) Nucleosynthetic W isotope anomalies and the Hf-W chronometry of Ca-Al-rich inclusions. *Earth Planet. Sci. Lett.* **403**, 317-327.

Kurat G. (1970) Zur genese der Ca-Al-reichen einschlüsse im chondriten von lancé. *Earth Planet. Sci. Lett.* **9**, 225-231.

Lodders K. (2003) Solar system abundances and condensation temperatures of the elements. *Astrophys. J.* **591**, 1220-1247.

Lu Q. and Masuda A. (1994) The isotopic composition and atomic weight of molybdenum. *Int J Mass Spectrom Ion Process* **130**, 65-72.

MacPherson G.J., Kita N.T., Ushikubo T., Bullock E.S., and Davis A.M. (2012) Well-resolved variations in the formation ages for Ca-Al-rich inclusions in the early Solar System. *Earth Planet. Sci. Lett.* **331-332**, 43-54.

Makide K., Nagashima K., Krot A.N., Huss G.R., Ciesla F.J. Hellebrand E., Gaidos E., and Yang L. (2011) Heterogeneous distribution of ^{26}Al at the birth of the solar system. *Astrophys. J.* 733, L31.

Martin P.M. and Mason B. (1974) Major and trace elements in the Allende meteorite. *Nature* **249**, 333-334.

Mason B. and Martin P.M. (1977) Geochemical differences among components of the Allende meteorite. *Smithson. Contrib. Earth Sci.* **19**, 84-95.

Mercer C., Souders A.K., Romaniello S.J., Williams C.D., Brennecka G.A., and Wadhwa M. (2015) Chromium and titanium isotope systematics of Allende CAIs. *Lunar Planet. Sci.* **46**, #2920.

Meteoritical Bulletin Database. 2016. https://www.lpi.usra.edu/meteor/. Accessed October 16, 2017.

Moreno T., Querol X., Castillo S., Alastuey A., Cuevas E., Herrmann L., Mounkaila M., Elvira J., and Gibbons W. (2006) Geochemical variations in Aeolian mineral particles from the Sahara-Sahel Dust Corrido. *Chemosphere* **65**, 261-270.

Moynier F., Day J.M.D., Okui W., Yokoyama T., Bouvier A., Walker R.J., and Podosek F.A. (2012) Planetary-scale strontium isotope heterogeneity and the age of volatile depletion of early Solar System materials. *Astrophys J* **758**, 45-52.

Papanastassiou D.A. (1986) Chromium isotopic anomalies in the Allende meteorite. *Astrophys. J.* **308**, L27-L30.

Paton C., Schiller M., and Bizzarro M. (2013) Identification of an ^{84}Sr-Depleted carrier in primitive meteorites and implications for thermal processing in the solar protoplanetary disk. *The Astrophysical Journal Letters* **763**, L40-L46.

Peters S. T. M., Münker C., Pfeifer M., Elfers B., and Sprung P. (2017) Distribution of p-process ^{174}Hf in early solar system materials and the origin of nucleosynthetic Hf and W isotope anomalies in Ca-Al rich inclusions. *Earth Planet. Sci. Lett.* **459**, 70-79.

Render J., Brennecka G. A., Kruijer T. S., and Kleine T. (2016) Hafnium isotopic compositions of refractory inclusions. *Goldschmidt 2016,* #2615.

Render J., Fischer-Gödde M., Burkhardt C., and Kleine T. (2017) The cosmic molybdenum-neodymium isotope correlation and the building material of the Earth. *Geochm. Persp. Let.* **3**, 170-178.

Russ G.P., Burnett D.S., Lingenfelter R.E., and Wasserburg G.J. (1971) Neutron capture on ^{149}Sm in lunar samples. *Earth Planet. Sci. Lett.* **13**, 53-60.

Russell, S.S. and Kearsley, A.T. (2011) A corundum-rich CAI from the Murchison (CM2) Meteorite. *LPI Contributions* **1639**, 9098.

Sahijpal S. and Goswami J.N. (1998) Refractory phases in primitive meteorites devoid of ^{26}Al and ^{41}Ca: representative samples of first solar system solids? *Astrophys. J.* **509**, L137-L140.

Scott E. R. D. (1984) Classification, metamorphism, and brecciation of type 3 chondrites from Antarctica. *Smiths. Contr. Earth Sci.* **26**, 73-94.

Simon S.B., Davis A.M., Grossman L., and McKeegan K.D. (2002) A hibonite-corundum inclusion from Murchison: A first-generation condensate from the solar nebula. *Meteorit. Planet. Sci.* **37**, 533-548.

Sprung P., Scherer E.E., Upadhyay D., Leya I., and Mezger, K. (2010) Non-nucleosynthetic heterogeneity in non-radiogenic stable Hf isotopes: Implications for early solar system chronology. *Earth Planet. Sci. Lett.* **295**, 1-11.

Stelzner TH., Heide K., Bischoff A., Weber D., Scherer P., Schultz L., Happel M., Schrön W., Neupert U., Michel R., Clayton R.N., Mayeda T.K., Bonani G., Haidas I., Ivy-ochs S., and Suter M. (1999) An interdisciplinary study of weathering effects in ordinary chondrites from the Acfer region, Algeria. *Meteoritics & Planet. Sci.* **34**, 787-794.

Telus M., Huss G.R., Ogliore R.C., Nagashima K., Howard D.L., Newville M.G., and Tomkins A.G. (2016) Mobility of iron and nickel at low temperatures: implications for ^{60}Fe-^{60}Ni systematics of chondrules from unequilibrated ordinary chondrites. *Geochim. Cosmochim. Acta* **178**, 87-105.

Trinquier A., Elliott T., Ulfbeck D., Coath C., Krot A.N., and Bizzarro M. (2009) Origin of nucleosynthetic isotope heterogeneity in the solar protoplanetary disk. *Science* **324**, 374-376.

Wark D.A. (1986) Evidence for successive episodes of condensation at high temperature in a part of the solar nebula. *Earth Planet. Sci. Lett.* **77**, 129-148.

Wark D.A. and Lovering J. F. (1977) Marker events in the early evolution of the solar system: Evidence from rims on Ca-Al-rich inclusions in carbonaceous chondrites. *Proc. Lunar Sci. Conf.,* **8**, 95-112.

Williams C. D., Janney P. E., Hines R. R., and Wadhwa M. (2016) Precise titanium isotope compositions of refractory inclusions in the Allende CV3 chondrite by LA-MC-ICPMS. *Chem. Geol*. **436**, 1-10.

Wood J.A. (1998) Meteoritic evidence for the infall of large interstellar dust aggregates during the formation of the solar system. *Astrophys. J.* **503**, L101-L104.

Yin Q., Jacobsen S.B., and Yamashita K. (2002) Diverse supernova sources of pre-solar material inferred from molybdenum isotopes in meteorites. *Nature* **415**, 881-883.

Yin Q.-Z., Sanborn M.E., and Zeigler K. (2017) Testing the common source hypothesis for CV and CK chondrites parent body using Δ^{17}O-ε^{54}Cr isotope systematics. *Lunar Planet. Sci.* **48**, #1771.